Dynamic simulations of coseismic slickenlines on non-planar and rough faults

T. Aoki [ORCID],[1] Y. Kaneko [ORCID][1] and J. Kearse [ORCID][2]

[1]*Graduate School of Science, Kyoto University, Kitashirakawa Oiwakecho, Sakyo Ward, Kyoto 606-8502, Japan. E-mail: aoki.takumi.28e@kyoto-u.jp*
[2]*School of Geography, Environment and Earth Sciences, Victoria University of Wellington, Kelburn, Wellington 6012, New Zealand*

SUMMARY

Knowing the directions of rupture propagation of palaeo-earthquakes is a challenging, yet important task for our understanding of earthquake physics and seismic hazard, as the rupture direction significantly influences the distribution of strong ground motion. Recent studies proposed a relationship between the direction of rupture propagation and curvature of slickenlines formed during seismic slip. The relationship was established using a global catalogue of historic surface-rupturing earthquakes and dynamic models of idealized, planar faults. At the same time, some slickenlines previously documented on geometrically complex fault segments show their convexity opposite from the simple model prediction, which we refer to as 'abnormal convexity'. To explain such observations, we perform simulations of spontaneous earthquake ruptures on non-planar and rough faults. We find that in the case of strike-slip faults, a non-planar fault model can lead to abnormal convexity of slickenlines in places where the fault dip angle changes abruptly from the average dip of the fault. Abnormal convexity of slickenlines is produced when the initial along-dip stresses are larger than, and are opposite in direction to, the dynamic stresses imparted by the mixed-mode rupture. Such results are also confirmed in our rupture simulations with a rough fault. Our results also show that the parameter space for which abnormal convexity of slickenlines occurs near Earth's surface is narrow, especially when the fault strength and initial shear stresses increase with depth. Nevertheless, slickenlines on geometrically complex faults need to be carefully interpreted and investigation of rupture direction using curved slickenlines should focus on structurally simple parts of faults.

Key words: Numerical modelling; Earthquake dynamics; Dynamics and mechanics of faulting; Palaeoseismology.

1 INTRODUCTION

Large earthquake ruptures often propagate unilaterally (McGuire *et al.* 2002), and in doing so influence the spatial distribution of strong ground motion (Somerville *et al.* 1997; Gomberg *et al.* 2001). This phenomenon is referred to as the directivity effect and has been observed in many large, strike-slip earthquakes, such as the 1992 M_w 7.3 Landers (California) earthquake (Ammon *et al.* 1993), the 1995 M_w 6.9 Kobe (Japan) earthquake (Yoshida *et al.* 1996), and the 2016 M_w 7.0 Kumamoto (Japan) earthquake (Kobayashi *et al.* 2017). Determining if there is systematic behaviour in the directions of rupture propagation on a given fault remains difficult due to short instrumental records (Andrews & Ben-Zion 1997; Harris & Day 2005), yet such knowledge may provide a useful constraint in seismic hazard analysis. While the rupture directions of modern earthquakes can be estimated from seismological observations, inferring the rupture direction of historic and prehistoric earthquakes

has been challenging. Previous studies utilize structural and geometrical data, such as off-fault damage patterns (Klinger *et al.* 2018) and branching fault intersection (Fliss *et al.* 2005). However, these methods have not been validated against the known rupture directions of large earthquakes.

Recent studies (Kearse *et al.* 2019; Kearse & Kaneko 2020) suggest a relationship between the direction of rupture propagation and the convexity of curved slickenlines engraved on fault surfaces. A slickenline, or a striation on a fault surface, records the history and slip direction at a point on the fault during seismic slip. Slickenlines are often found after large, surface-breaking earthquakes (Otsuki *et al.* 1997; Otsubo *et al.* 2013; Kearse *et al.* 2019). It has been shown that most slickenlines attributed to historical earthquakes are curved (Kearse & Kaneko 2020), suggesting that the slip direction temporally changes during a coseismic slip episode. Based on fault mechanics and numerical simulations, Spudich *et al.* (1998) and Guatteri & Spudich (1998) proposed that temporal changes in

slip directions are caused by dynamic stresses on the slipping fault surface. In their model, the transient stress changes occur along the mixed-mode rupture directions within a so-called process zone where the fault strength changes from the static to dynamic value. Kearse *et al*. (2019) and Kearse & Kaneko (2020) extended this concept and proposed that the sense of convexity of curved slickenlines depends on the rupture propagation direction. In particular, Kearse & Kaneko (2020) showed that the convexity of curved slickenlines in each of the eight historical earthquakes that have known rupture directions are consistent with those predicted by relatively simple dynamic rupture models. By modelling the well-documented curved slickenlines in the M_w 6.6 Fukushima earthquake in detail, Macklin *et al*. (2021) further showed that curved slickenlines may be also formed by the propagation of multiple rupture fronts, although the relationship between the sense of convexity and rupture direction remains the same as that predicted by models in which the main convexity is formed within the process zone of the propagating rupture. If such a relationship holds for pre-historic earthquakes, one may be able to infer the rupture directions of palaeo-earthquakes from fault trenching, as proposed by Kearse & Kaneko (2020).

At the same time, some previously documented slickenlines show a convexity that is opposite from the prediction of idealized models, which we refer to as 'abnormal convexity'. For example, following the M_w 7.8 Kaikoura (New Zealand) earthquake, slickenlines at 3 of 9 sites along the Kekerengu fault exhibit abnormal convexity (Kearse *et al*. 2019; Fig. 1). Since the rupture propagates towards the northeast direction, slickenlines on the Kekerengu fault predicted by idealized models are convex up (Fig. 1c), consistent with most observed slickenlines (Fig. 1a, Sites 2, 3, 4, 5, 6 and 8). As evident from Fig. 1(a), the sites corresponding to abnormal convexity are located at or in the vicinity of a fault bend or stepover (Fig. 1a, Sites 1, 7 and 9), and hence the local geometrical complexity may have influenced the convexity of slickenlines formed on the Kekerengu fault.

Geometrical complexity of faults manifested as fault non-planarity and roughness have previously been shown to influence the rupture dynamics and resulting ground motion (e.g. Harris & Day 1999; Dunham *et al*. 2011; Shi & Day 2013; Perrin *et al*. 2016; Ando & Kaneko 2018). Unlike planar faults, a non-planar fault subject to a uniform tectonic stress field induces a different direction of initial shear stresses on the non-planar fault segments, which may result in the convexity of slickenlines different from the prediction of planar fault models. Non-planar faults also lead to transient changes in normal stresses during the propagation of rupture. Since previous modelling studies of curved slickenlines are based on planar faults, it is important to understand potential complexity in the patterns of slip-path convexity arising from non-planar faults.

In this study, we examine if dynamic rupture models with non-planar and rough faults can produce abnormal convexity of slickenlines. We then assess under what conditions such abnormal convexity is generated in these models. In Section 2, we describe dynamic rupture model setups common to all the rupture scenarios shown in the subsequent sections. In Section 3, we analyse the slickenlines of simplified non-planar fault models with a uniform regional pre-stress. In Section 4, we show the results of simplified non-planar fault models with a more realistic, depth-dependent regional pre-stress. In Section 5, we consider models that incorporate fault roughness. Finally, we discuss the implications of our results for interpreting slickenlines observed in the field (Section 6).

2 MODEL SET-UP

We aim to construct and analyse a set of relatively simple models. To simulate spontaneous dynamic rupture on non-planar and rough faults, we consider a right-lateral, strike-slip fault in a homogeneous elastic half-space (Fig. 2a). The fault is governed by a linear slip-weakening friction law (Ida 1972; Palmer & Rice 1973), where the friction coefficient decreases from its static value μ_s to a dynamic value μ_d over characteristic slip d_c. We assume a uniform or depth-dependent tectonic stress field, which induces non-uniform initial stresses on non-planar fault segments (Fig. 2b). To initiate earthquake rupture on the fault, we impose an additional shear stress in a circular zone around the hypocentre. Once the rupture nucleates, it spontaneously propagates over the fault outside the circular nucleation zone. We use a spectral-element code (Ampuero 2002; Kaneko *et al*. 2008), which has been verified through a series of community benchmark exercises (Harris *et al*. 2018). The details of the friction law implementation and numerical resolution are described in Appendix A.

3 NON-PLANAR FAULT MODEL WITH UNIFORM REGIONAL PRE-STRESS

3.1 Model set-up

We first consider an idealized model of a 36-km-long and 15-km-deep, non-planar, right-lateral strike-slip fault subject to a uniform regional pre-stress. We closely follow the problem formulation of TPV28 in the SCEC/USGS benchmark (Harris *et al*. 2018), but modify the fault geometry and the location of the hypocentre. The strike-slip fault extends horizontally from $x = -28$ km to $x = 8$ km, as we consider the left-hand side of the fault with respect to the hypocentre located at $x = 0$. The uniform regional pre-stress, expressed as a stress tensor σ, is given by

$$\sigma[\text{MPa}] = \begin{pmatrix} \sigma_{11} & \sigma_{12} & \sigma_{13} \\ \sigma_{12} & \sigma_{22} & \sigma_{23} \\ \sigma_{13} & \sigma_{23} & \sigma_{33} \end{pmatrix} = \begin{pmatrix} -60.00 & 29.38 & 0 \\ 29.38 & -60.00 & 0 \\ 0 & 0 & 0 \end{pmatrix}, \qquad (1)$$

where a negative sign denotes compression, and 1, 2 and 3 directions are x, y and z directions shown in Fig. 2(a), respectively. This regional stress field is optimal for a vertical, right-lateral, strike-slip fault in a sense that the dip-slip shear stress on the planar part of the fault is zero. The non-planar fault consists of a 10-km-long shallow (<1.5 km depth) protruded segment and otherwise a planar, 36-km-long and 15-km-deep vertical segment (Fig. 3a). Initial shear and normal stresses on the fault are calculated by resolving the stress tensor onto the fault surface (Appendix B). The protruded fault segment subject to the uniform stress field leads to non-zero components of the shear tractions resolved on the fault plane (Fig. 3b). We set the hypocentre at the right-hand side of the fault (Fig. 3a) and analyse synthetic slickenlines at the left-hand side of the hypocentre, motivated by the northeastward rupture propagation direction on the Kekerengu fault (Fig. 1a). Parameters assumed in this model are listed in Table 1.

3.2 Slickenlines in simple non-planar fault model with uniform regional pre-stress

We find that non-planar fault models can result in abnormal convexity of slickenlines on the non-planar fault segment. Fig. 4(a) shows a
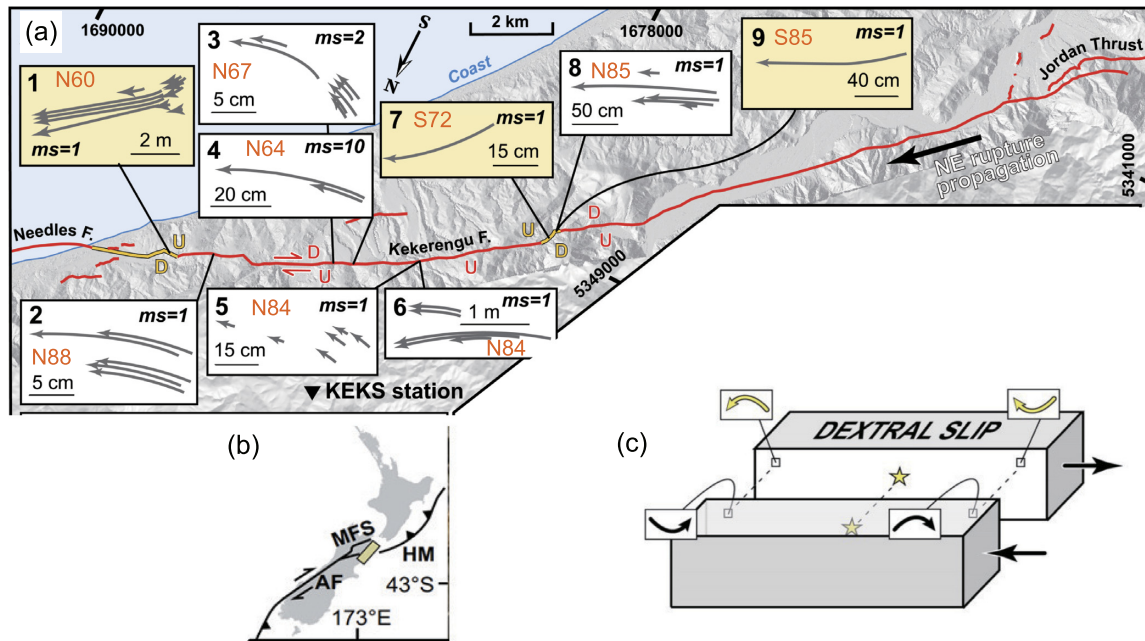
Figure 1. Curved slickenlines observed on the Kekerengu fault following the M_w 7.8 Kaikoura earthquake. (a) The map of the Kekerengu fault and slickenlines documented in Kearse *et al.* (2019). Each box shows the observation site and grey arrows are slickenlines documented at each site. Slickenlines are observed on the southeastern side of the Kekerengu fault. A black arrow shows the direction of rupture propagation (Holden *et al.* 2017). Numbers in orange with S or N represent local dip angles, and S or N corresponds to southeast or northwest dip direction, respectively (Kearse *et al.* 2018). Most slickenlines observed along the Kekerengu fault have convex-up curvature, consistent with the planar fault model of Kearse *et al.* (2019). Some slickenlines show convex-down curvature (Sites 1, 7 and 9). This 'abnormal convexity' of slickenlines is found at or in the vicinity of a fault bend or stepover. (b) The map of New Zealand. The rectangular box shows the region in Fig. 1(a). (c) The schematic diagram of curvature of slickenlines on a planar, right-lateral strike-slip fault (Kearse & Kaneko 2020). Yellow and black arrows are slickenlines on the far and near sides of the fault, respectively.

dynamic rupture scenario with the amplitude of the protruded fault $A = 300$ m (in other words, the width of the protruded fault step is 300 m at the surface). When the rupture nucleates and propagates on the planar fault region, the slip direction of the mixed-mode rupture changes temporally (Fig. 4a). In this case, vertical shear stresses generated by the slip in the process zone of the rupture front cause the temporal change of the slip direction (Spudich *et al.* 1998). However, as the rupture front reaches the non-planar fault segment, the instantaneous slip direction becomes different from that of the planar-fault model (Compare Figs 2c and 4a). The resulting curved slickenlines on the non-planar fault segment are convex down, opposite from the planar-fault counterpart (Fig. 4b). The initial vertical shear stress acting on the non-planar fault segment produces a large vertical slip rate during the earlier part of the slip-path while the horizontal slip rate decelerates more slowly (Fig. 4c), leading to convex-down slickenlines. This abnormal convexity occurs because the non-zero vertical pre-stress induced by the protruded fault segment is of larger magnitude, and acting in the opposite sense than the transient vertical stresses imparted by the mixed mode rupture.

To eliminate the effect of complexity arising from the non-planar geometry, we consider a planar fault model and assume the same initial shear and normal stress distributions on a planar fault as in the non-planar fault model (Figs 5a and b). In this case, the resulting slickenlines are nearly identical to those in the non-planar fault model (compare Figs 4b and 5c). This means that the change of slickenline curvature is caused not by the fault geometry directly, but by the initial shear stresses on the fault induced by the non-

planar fault geometry. This result suggests that a distribution of initial dip-slip shear stresses significantly influences the convexity of slickenlines engraved on strike-slip faults. It also shows that transient changes in normal stresses induced by non-planar fault geometry do not affect the slickenline curvature. Note that this inference holds when the amount of slip is very small compared to the roughness wavelength (e.g. Dunham *et al.* 2011).

To assess the effect of non-planar fault geometry on the resulting slickenline curvature, we consider non-planar models with different amplitude A of the protruded fault segment (Fig. 6). As the initial vertical shear stress is an important parameter, we also report the ratio of the initial vertical shear stress to initial horizontal shear stress τ_{ds}^0/τ_{ss}^0 on the non-planar fault segment in each scenario (Fig. 6). When the non-planar fault segment protrudes towards the far side of the model, A is positive. In those cases, the curvature of convex-up slickenline is enhanced compared to the planar fault counterpart due to the vertical pre-stress and transient stresses in the rupture process zone acting in the same direction (which produces a large negative τ_{ds}^0/τ_{ss}^0, Fig. 6). In contrast, a non-planar fault segment protruded towards the near side of the model (i.e. negative A) leads to a more straight slickenline for moderately negative values of A, or convex-down slickenline for a large negative value of A. In those cases, a downward initial vertical shear stress, or large τ_{ds}^0/τ_{ss}^0, promotes the convex-down curvature (Fig. 6). Hence, the degree of slickenline curvature and the occurrence of abnormal convexity depend on τ_{ds}^0/τ_{ss}^0 controlled by the degree of fault non-planarity on the strike-slip fault.
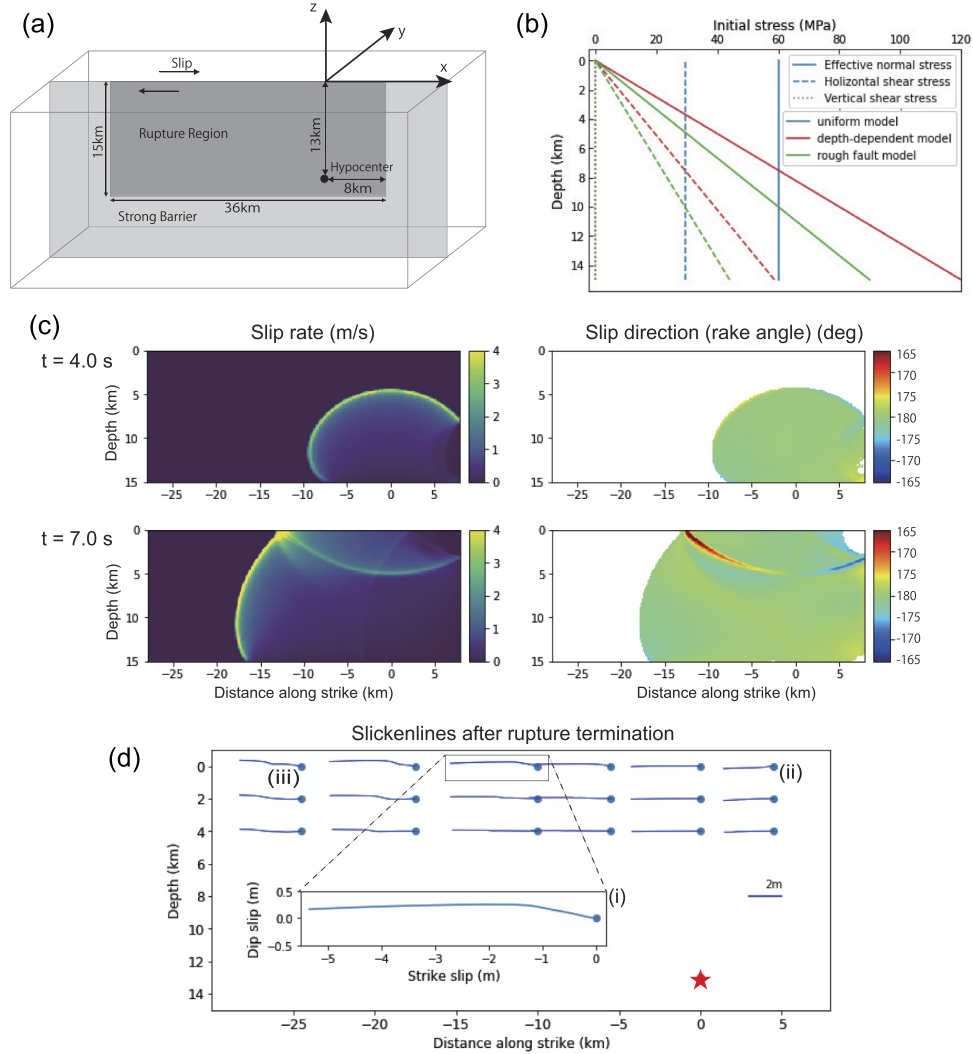
Figure 2. Curved slickenlines predicted by a simple, planar fault model. (a) The set-up of a planar, right-lateral, strike-slip fault model. A dark grey area shows the rupture region and a light grey area corresponds to the region of an unbreakable rupture barrier. (b) Initial stress distributions resolved onto the planar fault. Blue and red lines correspond to values assumed for non-planar fault models with uniform (Section 3) and depth-dependent (Section 4) tectonic stress fields, respectively. Green lines correspond to values assumed for rough fault models (Section 5). Solid lines are effective normal stresses, dashed lines are horizontal shear stresses, and dotted lines are vertical shear stresses on the fault. (c) Snapshots of slip rate (left-hand panels) and instantaneous slip direction (right-hand panels). (d) Simulated slickenlines on the planar fault. Each blue line is a slickenline engraved on the far side of the fault, which is calculated at each blue dot on the fault plane, and a red star shows the hypocentre. Location (i) is the slickenline at $(x, z) = (-10\,\text{km}, 0\,\text{km})$, and Location (ii) is the slickenline at $(x, z) = (5\,\text{km}, 0\,\text{km})$. Slickenlines on the left-hand side of the hypocentre [e.g. location (i)] show convex-up and the right-hand side [e.g. (i)] is convex-down. Location (iii) is the slickenline at $(x, z) = (-24.5\,\text{km}, 0\,\text{km})$, which has a complex shape due to the development of free-surface-induced supershear rupture (Macklin *et al.* 2021).

4 NON-PLANAR FAULT MODEL WITH DEPTH-DEPENDENT REGIONAL PRE-STRESS

4.1 Model set-up

Next, we consider models with more realistic, depth-dependent regional pre-stress, where the initial stress tensor σ is defined by

$$\sigma\,[\text{MPa}] = \begin{pmatrix} \sigma_{11} & \sigma_{12} & \sigma_{13} \\ \sigma_{12} & \sigma_{22} & \sigma_{23} \\ \sigma_{13} & \sigma_{23} & \sigma_{33} \end{pmatrix} = \begin{pmatrix} -60.00 & 29.38 & 0 \\ 29.38 & -60.00 & 0 \\ 0 & 0 & 0 \end{pmatrix} \times \frac{|z|}{7.5\,\text{km}} \quad . \quad (2)$$

We consider a non-planar fault geometry (Fig. 7a) similar to those shown in Section 3. The depth-dependent stress tensor induces depth-dependent, initial shear and normal stresses on the fault (Figs 2b and 7b). As in the uniform regional stress scenario, the initial vertical shear stresses are non-zero on the non-planar fault segment (Fig. 7b).

4.2 Slickenlines in simple non-planar fault model with depth-dependent regional pre-stress

In the case of depth-dependent regional pre-stress, the initial stresses on the fault are close to zero near the Earth's surface, and the effect of fault non-planarity on slickenline curvature diminishes at shallow depths. Fig. 8 shows a representative case with depth-dependent regional pre-stress in which abnormal convexity forms.
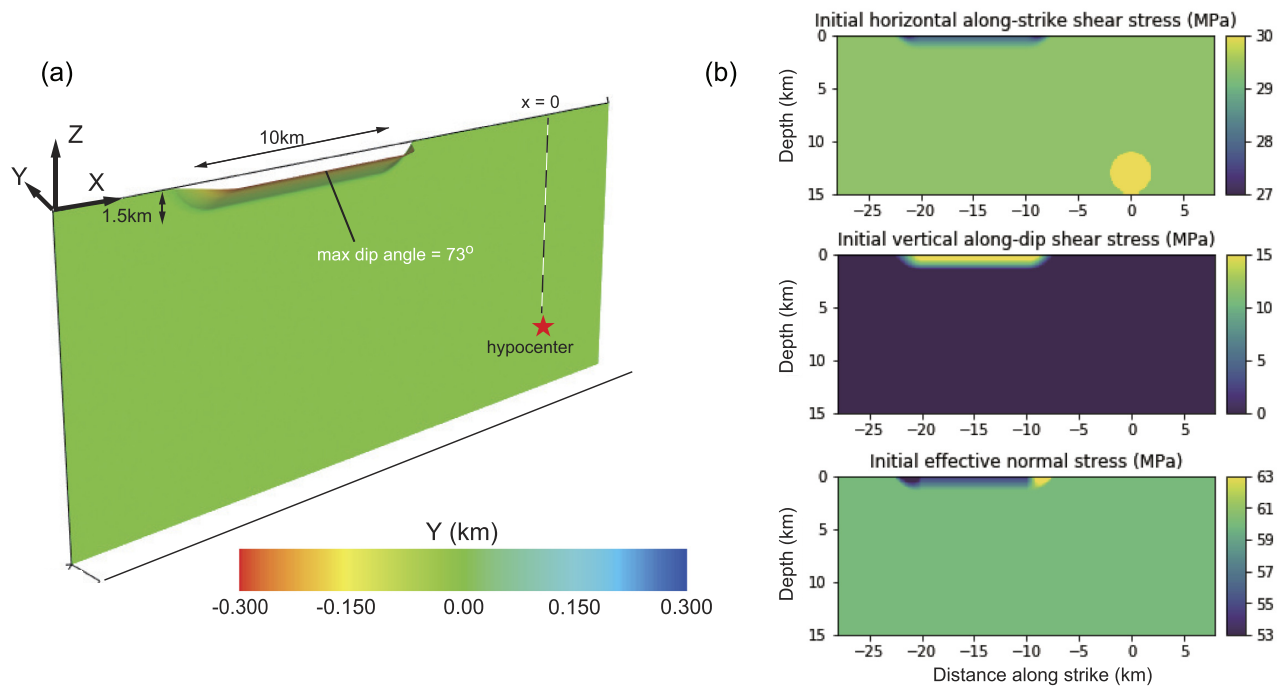
Figure 3. Model setup and the distribution of initial stresses on a non-planar fault model with uniform regional pre-stress. (a) Fault geometry. The non-planar fault segment is characterized by a 10-km-long and 1.5-km-deep protruded region. In this figure, the amplitude A of the protruded region at the Earth's surface is −300 m, which is horizontally exaggerated for the illustration purpose. (b) Along-strike component of initial shear stress, along-dip component of initial shear stress, and initial effective normal stress on the fault. A yellow circle corresponds to the circular nucleation patch. On the non-planar fault segment, the initial stresses are different from those on the planar fault segment.

Table 1. Model parameters assumed in this study.

	Parameter	Non-planar fault with uniform regional pre-stress	Non-planar fault with depth-dependent regional pre-stress	Rough fault with depth-dependent regional pre-stress
ρ	Density	2670 kg m^{-3}	2670 kg m^{-3}	2670 kg m^{-3}
α	P-wave velocity	6000 m s^{-1}	6000 m s^{-1}	6000 m s^{-1}
β	S-wave velocity	3464 m s^{-1}	3464 m s^{-1}	3464 m s^{-1}
μ_s	Static friction	0.677	0.677	0.677
μ_d	Dynamic friction	0.373	0.25–0.373	0.373–0.52
d_c	Slip-weakening distance	0.30–0.40 m	0.30–0.60 m	0.40 m
C_0	Frictional cohesion in the top 5 km	0–1 MPa	0–5 MPa	0–1 MPa

In this case, the degree of fault non-planarity ($A = -1.4$ km and the depth extent of 3.0 km) is set to be larger than those considered in Section 3 (Fig. 7a). To prevent rupture nucleation at the start of the simulation within the protruded fault segment resulting from large initial shear stresses there, we impose frictional cohesion $C_0 = 3$ MPa over $|z| < 5$ km on the fault. Note that the assumed value of C_0 may be larger than typical frictional cohesion ($C_0 \sim 0.1$ MPa; Harris *et al.* 2018), and hence C_0 is varied in models discussed in the subsequent section. As in the case with uniform regional pre-stress, the local slip direction changes when the rupture reaches the non-planar segments (Fig. 8a), resulting in abnormal convexity of slickenlines (Fig. 8b). The maximum convex-down curvature occurs at a depth of 1.5 km, where the ratio τ_{ds}^0/τ_{ss}^0 is the largest, consistent with the result shown in Section 3. Slickenlines in the planar fault segment deeper than 3 km are convex up, as expected from the planar-fault model.

4.3 Parameter sensitivity of abnormal convexity

To assess a range of model parameters over which abnormal convexity is produced, we consider a total of 37 cases with a different combination of A and frictional cohesion C_0. To quantify the curvature of synthetic slickenlines, we fit two straight lines to each curved slickenline as follows. Given that the initiation and termination points of a slickenline are known, we define another point along the curved slickenline and connect these three points, which form two straight lines (e.g. red and orange lines in Fig. 9a). We then vary the location of the middle point along the curved slickenline, calculate the residual between the two straight lines and curved slickenline using the method of least squares, and find the best-fitting straight lines and corresponding angle θ between them (Fig. 9a). When a slickenline has convex-up curvature, θ is greater than 180°, whereas for a convex-down slickenline, θ is smaller than 180°.
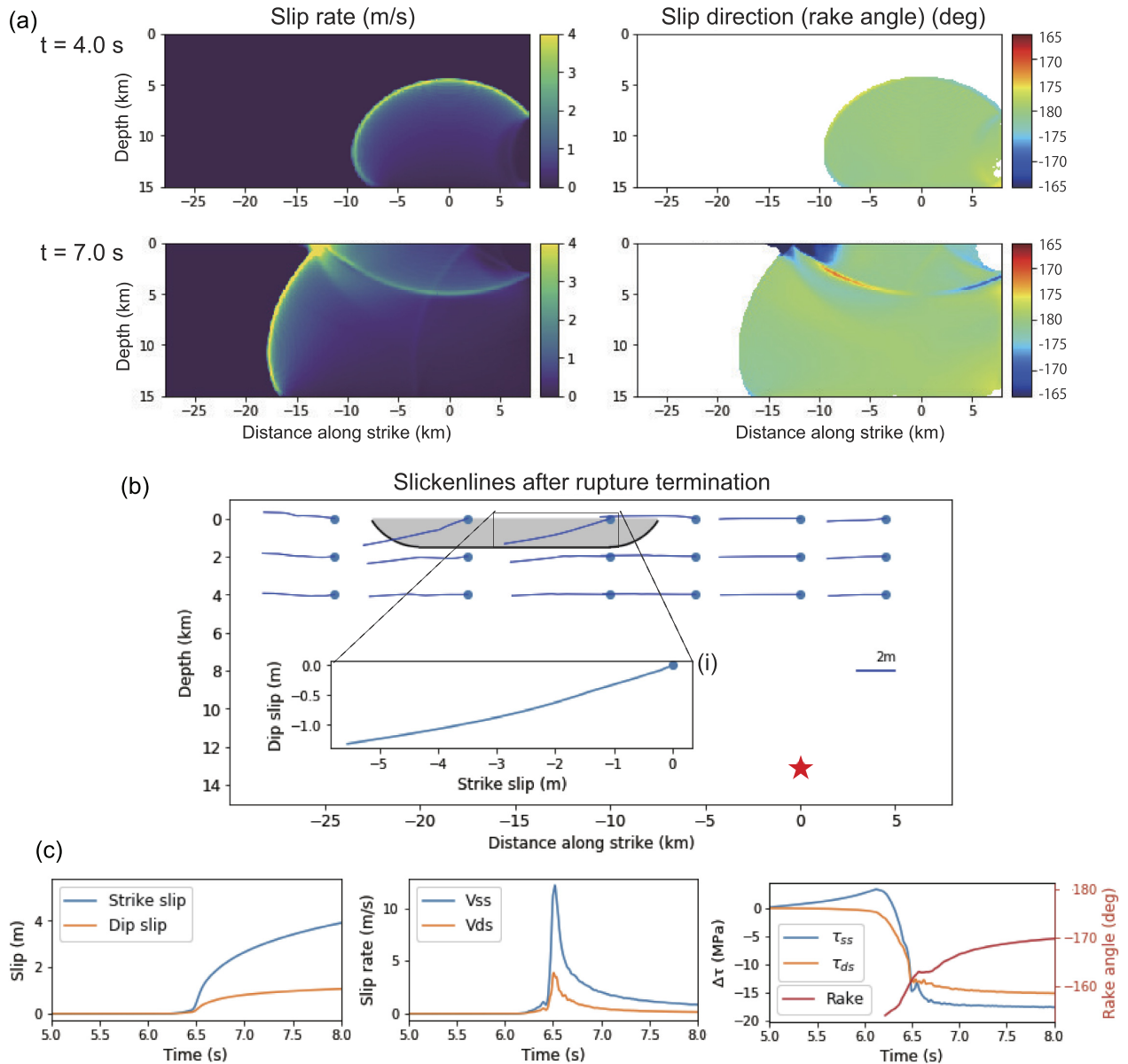
Figure 4. Curved slickenlines in the non-planar fault model with uniform regional pre-stress shown in Fig. 3 and with $d_c = 0.40$ m and $C_0 = 0$ MPa. (a) Snapshots of slip rates and instantaneous slip direction at each time step. When the rupture reaches the non-planar fault segment, the local slip direction becomes different from those in the planar fault model shown in Fig. 2. (b) Synthetic slickenlines engraved on the far side of the fault in the non-planar fault model. A grey area corresponds to the non-planar fault segment. The inset panel shows a zoom-in of the convex down slickenline at location (i) $(x, z) = (-10$ km, 0 km) (i.e. abnormal convexity). (c) Plots of slip (m), slip rates (m s^{-1}), and shear traction changes (MPa) at location (i). V_{ss} and V_{ds} correspond to strike-sip and dip-slip slip rates, respectively, and τ_{ss} and τ_{ds} are along-strike and along-dip components of shear stress changes, respectively. The rake angle in this plot is smoothed by a moving average with the window size of 0.2 s.

We find that the parameter space for which abnormal convexity of slickenlines occurs near the Earth's surface is narrow. A majority of cases shown in Fig. 9(b) show θ greater than 180° at the Earth's surface. In several instances where A is large negative and C_0 is small, the rupture spontaneously nucleates from the protruded fault segment where the initial shear stress magnitude exceeds the shear strength. These cases are deemed unrealistic, as large earthquakes rarely nucleate at shallow depths. Abnormal convexity occurs when A is large and C_0 is unrealistically large, as in Fig. 8. At slightly deeper regions (>0.5 km depth), abnormal convexity forms over a wide range of parameters (Figs 9c and d). These results suggest that

it may be uncommon to see abnormal convexity of slickenlines near the Earth's surface by geologists.

To analyse the dependence of slickenline curvature on other friction parameters, we vary slip-weakening distance d_c and dynamic friction coefficient μ_d. Fig. A2 shows synthetic slickenlines at $(x, y, z) = (-10$ km, A, 0 km) and $(-10$ km, A, -1 km) with $A = -400$ m and $C_0 = 1$ MPa in the non-planar fault model with depth-dependent regional pre-stress. We find that varying d_c by up to a factor of 2 does not significantly change the slickenline curvature (Fig. A2). Cases with $d_c = 60$ cm and greater lead to rupture arrest soon after it nucleates. Varying μ_d results in different
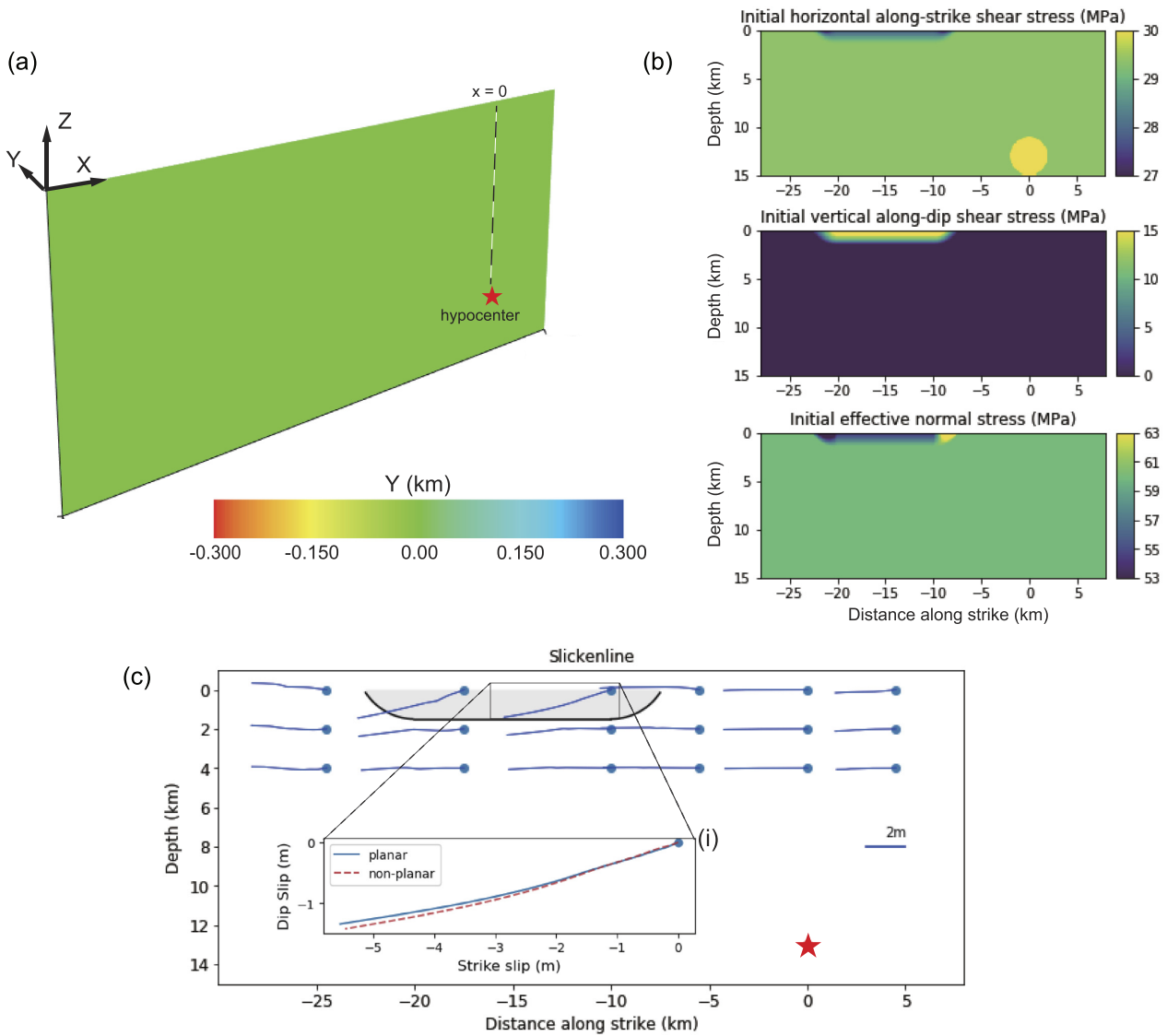
Figure 5. Model setup and slickenlines in a planar fault model with the initial stress distribution derived from the non-planar fault with uniform regional pre-stress shown in Fig. 3. (a) Fault geometry, which is the same as in Fig. 2(a). The hypocentre (red star) is located at $z = -7.5$ km. (b) Initial stresses on the fault that are identical to Fig. 3(b). (c) Synthetic slickenlines engraved on the far side of the fault in this planar fault model. A patch of the non-uniform initial stresses indicated by a light grey area shows abnormal slickenlines, nearly identical to those shown in Fig. 4(b). A red dashed line represents the synthetic slickenline from Fig. 4(b, i).

amount of total slip and the degree of slickenline curvature while the convexity remains unchanged (Fig. A2). These results are qualitatively consistent with the results of previous studies (Kearse *et al.* 2019; Macklin *et al.* 2021).

5 ROUGH FAULT MODEL WITH DEPTH-DEPENDENT REGIONAL PRE-STRESS

5.1 Model set-up

We further consider models with more realistic fault geometry by assuming a rough fault with depth-dependent regional pre-stress. We assume a 20 km by 40 km fault with the roughness considered in benchmark problem TPV29 of Harris *et al.* (2018; Fig. 10a). In

this fault geometry, self-similar roughness is generated by a linear superposition of randomly selected sine waves, with each sine wave having a 1–40 km wavelength, and an amplitude equal to the square of the wavelength. The surface is then smoothed by a moving-average filter with a radius of 1 km, to eliminate wavelengths too short to be numerically resolved. We set the hypocentre at 10 km depth and consider a depth-dependent regional stress field given by

$$\sigma \,[\text{MPa}] = \begin{pmatrix} \sigma_{11} & \sigma_{12} & \sigma_{13} \\ \sigma_{12} & \sigma_{22} & \sigma_{23} \\ \sigma_{13} & \sigma_{23} & \sigma_{33} \end{pmatrix} = \begin{pmatrix} -60.00 & 29.38 & 0 \\ 29.38 & -60.00 & 0 \\ 0 & 0 & 0 \end{pmatrix} \times \frac{|z|}{10\,\text{km}} . \quad (3)$$

Note that the initial stresses acting on the planar part of the fault at 10 km depth are the same as those at 7.5 km depth in Section 4.
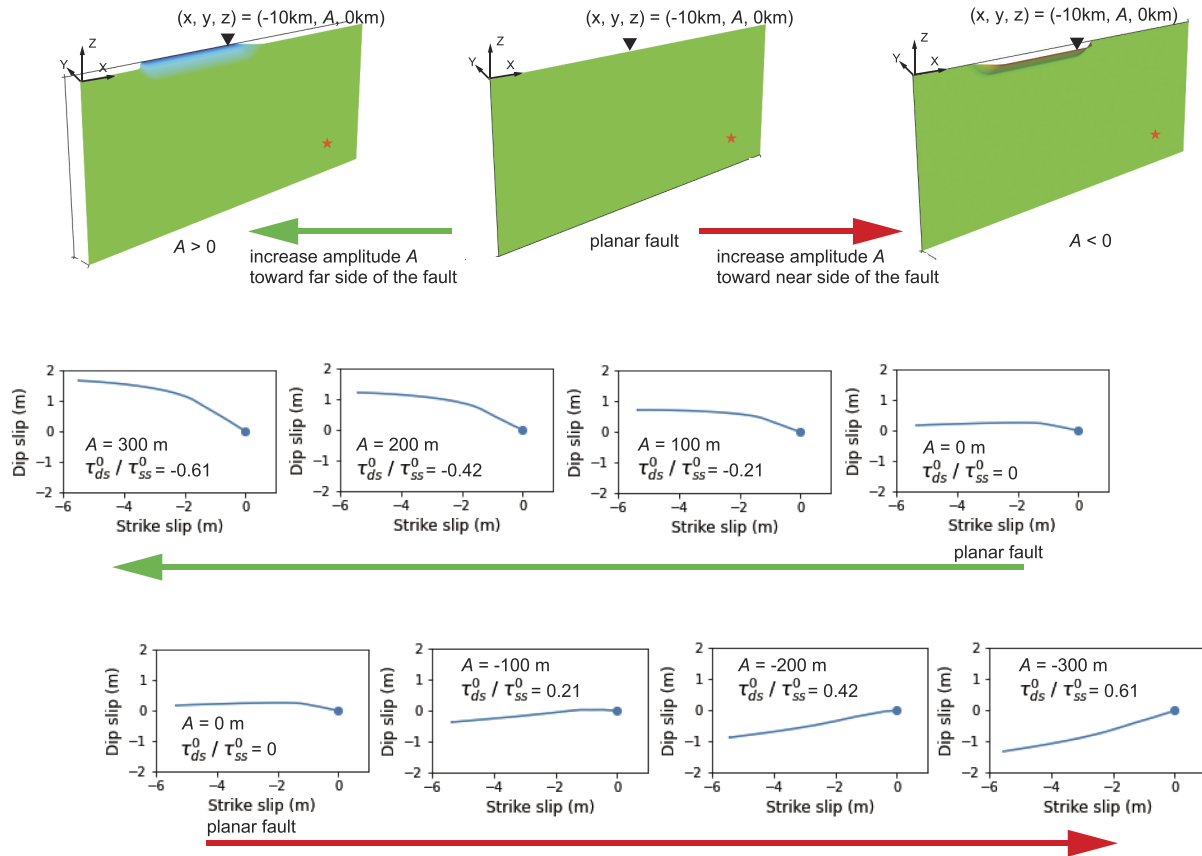
Figure 6. The dependence of slickenline curvature on the amplitude of non-planar fault geometry. The model parameters are $d_c = 0.40$ m and $C_0 = 0$ MPa. Parameter A is defined as the amplitude of the displaced fault at the Earth's surface along the y-axis. Top three panels show how the fault geometry is modified with respect to A. The middle and bottom panels are synthetic slickenlines engraved on the far side of the fault at $(x, y, z) = (-10$ km, A, 0 km$)$ in the models with different A, with $A = 0$ m corresponds to the planar fault. Cases with increasing A towards the far side of the fault lead to more pronounced, convex-up slip-path curvature. In contrast, cases with decreasing A (i.e. towards near side of the fault) show how the slip-path convexity changes from convex-up curvature to convex-down curvature. τ_{ds}^0/τ_{ss}^0 is the ratio of initial vertical along-dip stress τ_{ds}^0 to initial horizontal along-strike stress τ_{ss}^0 at $(x, y, z) = (-10$ km, A, 0 km$)$.

5.2 Slickenlines in rough fault model with depth-dependent regional pre-stress

We find that the rough fault models complicate the spatial pattern of slickenline convexity while the main features are consistent with those of simpler models shown in previous sections. Fig. 10 shows the fault geometry, rupture arrival time and synthetic slickenlines in a representative rough fault model. Grey and white regions in Fig. 10(c) correspond to convex-up and convex-down slickenline curvature expected from a planar fault model, respectively. Along the boundaries of these regions corresponding to Mode II and III rupture directions, the slickenlines are curved unlike in the planar fault model (Fig. 2d), due to the complex rupture propagation path in the rough fault scenario (Fig. 10c). In the grey and large positive τ_{ds}^0/τ_{ss}^0 (red colour contour) area [(iv) in Fig. 10c], slickenlines at depths tend to be convex down (i.e. abnormal convexity). Similarly, slickenlines in the white and large negative τ_{ds}^0/τ_{ss}^0 (blue colour contour) area [(v) and (vi) in Fig. 10c] are convex up (i.e. abnormal convexity). However, at shallow depths (<2.5 km), the slickenline convexity is the same as in the planar fault model due to relatively small absolute stresses there, consistent with the result of Section 4.

We further consider three additional rough fault models with a different degree of fault roughness: $0.5 \times A_{rough}$, $1.5 \times A_{rough}$ and $-1.5 \times A_{rough}$ (Fig. 11), where A_{rough} is defined as the y-axis positions

of the rough fault shown in Fig. 10. Even in these cases, the results are similar to the case shown in Fig. 10. Near the Earth's surface, the convexity of slickenline curvature is the same as in the planar fault model. Abnormal convexity may form at depths where the local value of τ_{ds}^0/τ_{ss}^0 is positively or negatively large depending on the locations of the slickenlines relative to the hypocentre (Fig. 11). The effect of fault roughness on the pattern of slickenline convexity is strong when the fault is rougher, and the ratio of initial shear stresses induced by local change of fault geometry controls the convexity of slickenline curvature at depths (Fig. 11).

6 DISCUSSION

6.1 Interpreting abnormal slickenlines on the Kekerengu fault

Our modelling results suggest that abnormal convexity of slickenlines may form along fault segments where the local fault geometry changes abruptly. In particular, abnormal convexity of slickenlines is produced in places along the fault where the initial along-dip stresses are larger than, and are opposite in direction to, the dynamic stresses imparted by the mixed-mode rupture. In the case of a strike-slip fault, the ratio of the initial vertical to the horizontal
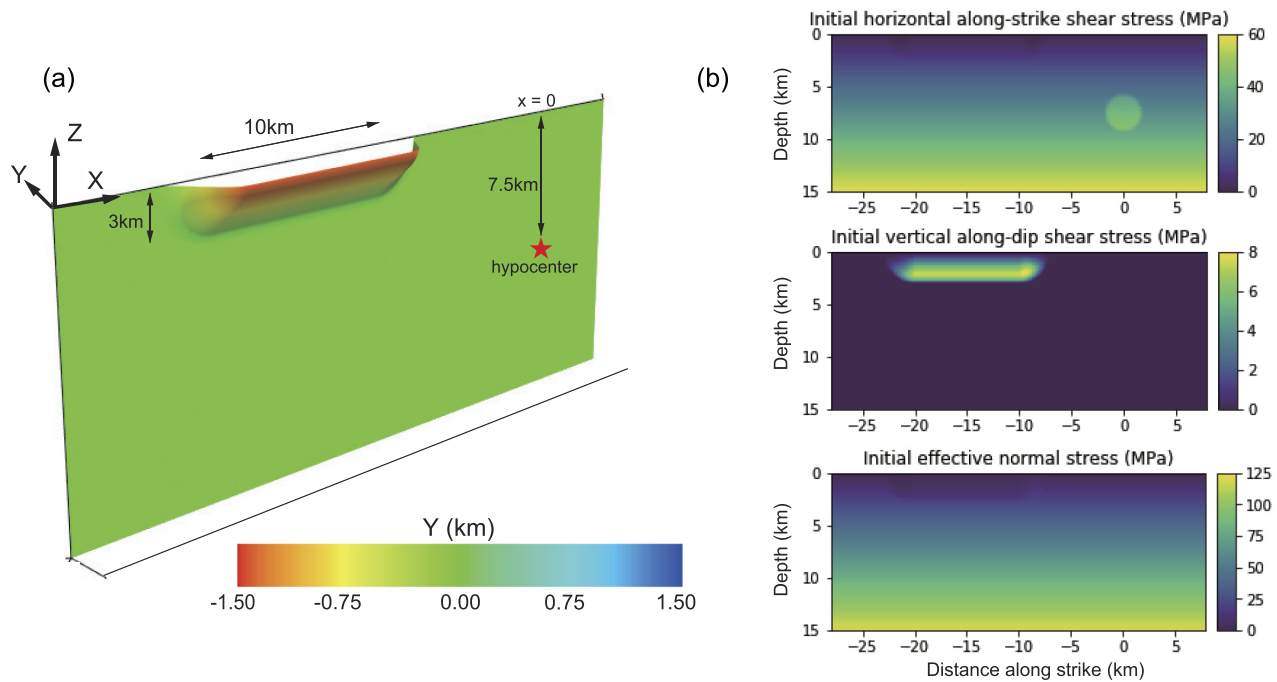
Figure 7. Set-up of a non-planar fault model with depth-dependent regional pre-stress. (a) The geometry of the non-planar fault, with $A = -1.4$ km and the depth of the non-planar segment is 3 km. Note that the degree of non-planarity is larger than that shown in Fig. 3(a). (b) Depth-dependent initial stresses resolved onto the fault.

shear stress τ_{ds}^0/τ_{ss}^0 depends significantly on the local dip angle and dip direction of the fault.

On the Kekerengu fault after the Kaikoura earthquake, abnormal slickenlines were observed at fault bends or stepovers (Fig. 1). Field observations suggest that one of the fault segments where abnormal convexity was observed dips towards the southeast while the majority of the Kekerengu fault dips steeply towards the northwest (Kearse *et al.* 2019; Sites 7 and 9 in Figs 1a, and 12). This local change of the dip angle indicates that τ_{ds}^0/τ_{ss}^0 on this fault segment would have been different from the majority of the Kekerengu fault. Based on our modelling results, the sense of curvature change needed to induce the observed abnormal convexity is consistent with the dip direction changes documented by the field observations (Fig. 12). Although the exact dip angle and the depth extent of this fault segment is unknown and more thorough investigation may be warranted, our results suggest that an abrupt change in a fault dip angle can lead to abnormal convexity of slickenlines.

In contrast, Site 1 (Fig. 1a) shares the same dip direction as the average dip on the Kekerengu fault, yet is located within an extensional stepover. At this location, subsidence of the northwest-side of the fault (the hanging wall) produces the opposite sense of dip slip to the main part of the Kekerengu fault, consistent with the kinematics of an extensional fault stepover. Given the local dip direction at Site 1, our modelling results indicate that the dip-slip pre-stress resolved onto this fault segment should have induced slight thrust motion and would not give rise to the abnormal convexity observed in the field (Fig. 6). We speculate that the rupture along this short fault segment may have propagated towards the southwest direction (opposite from the overall rupture direction), or that the extensional fault stepover characterized by a dipping, connecting fault may have induced a complex, dynamic stress field that was not accounted in our present model. Regardless of the mechanism, the abnormal convexity of slickenlines at Site 1 was likely caused by the structural complexity of the fault.

6.2 Occurrence of abnormal slickenlines under a limited range of conditions

We find that abnormal convexity rarely occurs near the Earth's surface in non-planar and rough-fault models with depth-dependent regional pre-stress. Since the initial shear stresses at shallow depths (<0.2 km) are much smaller than those at greater depths, the curvature of slickenlines would not change with respect to the prediction of the planar fault model. This inference is consistent with the paucity of abnormal slickenlines found in a global study (Kearse & Kaneko 2020). At the same time, our results also indicate that abnormal slickenlines may form in places where the fault geometry changes abruptly (Figs 8 and 9). In addition, Abnormal convexity might be more common along geometrically complex faults at a few kilometre depths where the initial shear stresses are much larger than that near the Earth's surface (Fig. 8c), although geologists do not generally have access to fault surfaces at depths.

6.3 Effect of velocity-strengthening frictional behaviour at shallow depths

Geophysical, geological and laboratory studies indicate that the shallow (<2– km) portion of the fault is characterized by velocity-strengthening frictional behaviour (Marone e*t al.* 1991; Marone 1998). To assess the influence of velocity-strengthening frictional behaviour at shallow depths on the resulting slickenlines in the framework of a slip-weakening friction law, we consider the model with the negative stress drop patch located within the top 3 km of the fault (e.g. Pitarka *et al.* 2009). With respect to the positive stress drop slip-weakening only model, synthetic slickenlines in the model with the shallow negative stress drop slip-weakening patch are smoother while the overall shape and curvature of the slickenlines remain unchanged (Fig. 13). This implies that the convexity of slickenlines
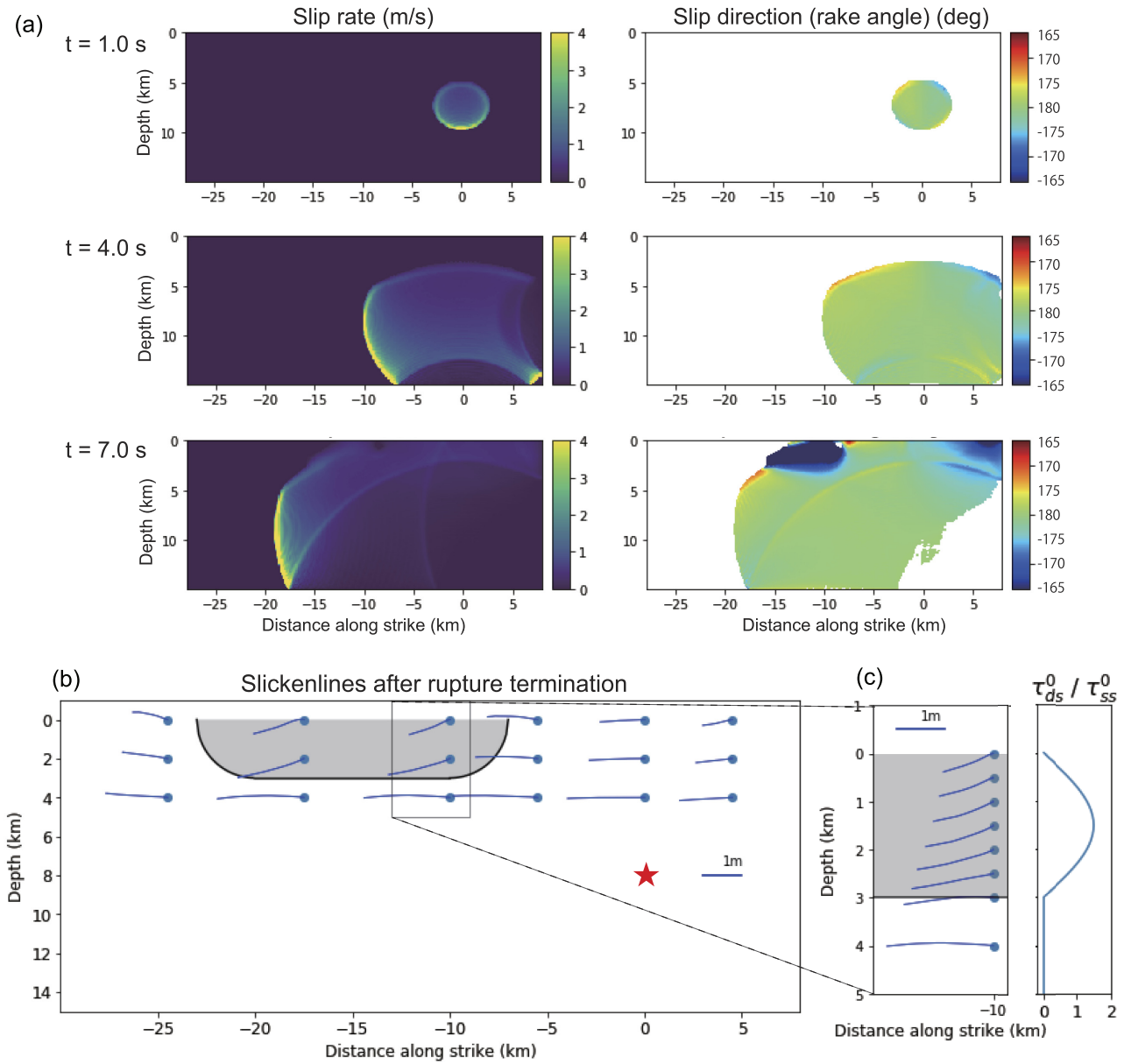
Figure 8. Curved slickenlines in the non-planar fault model with depth-dependent regional pre-stress shown in Fig. 7. Model parameters assumed in this case are $\mu_d = 0.25$, $d_c = 0.40\,\text{m}$, and $C_0 = 3\,\text{MPa}$ at $|z| < 5\,\text{km}$. (a) Snapshots of slip rate ($\text{m\,s}^{-1}$) and instantaneous slip direction (°) on the fault. (b) Synthetic slickenlines engraved on the far side of the fault in this non-planar fault model. A grey area corresponds to the non-planar fault segment. Some slickenlines in the grey area have abnormal convexity. (c) A zoom-in plot focusing on the depth distribution of slickenlines, and the corresponding ratio of initial along-dip shear stress τ_{ds}^0 to initial along-strike shear stress τ_{ss}^0. The region of larger τ_{ds}^0/τ_{ss}^0 shows enhanced convex-down curvature.

may be insensitive to whether the shallow portion of the fault is slip-weakening or velocity-strengthening.

6.4 Occurrence of abnormal slickenlines on dip-slip or oblique-slip faults

Our results suggest that the ratio of initial vertical to horizontal shear stresses τ_{ds}^0/τ_{ss}^0 is an important parameter in controlling the convexity of slickenlines on strike-slip faults (Figs 9–11). Since faults in nature also include dip-slip and oblique-slip faults, we also extend our analysis to those faults. Let us define $\bar{\theta}_0$ as the average

rake angle of pre-stress direction on the fault as follows:

$$\bar{\theta}_0 = \tan^{-1}\left(\frac{\bar{\tau}_z^0}{\bar{\tau}_x^0}\right), \tag{4}$$

where $\bar{\tau}_z^0$ and $\bar{\tau}_x^0$ are average initial vertical and horizontal shear stresses, respectively. At a given point on the fault, the local values of shear stresses, τ_z^0 and τ_x^0, may be different from the average values. Then the deviation angle $\Delta\theta_0(x, z)$, which is the difference between the local pre-stress direction and $\bar{\theta}_0$, is given by

$$\Delta\theta_0(x, z) = \tan^{-1}\left(\frac{\tau_z^0}{\tau_x^0}\right) - \bar{\theta}_0. \tag{5}$$
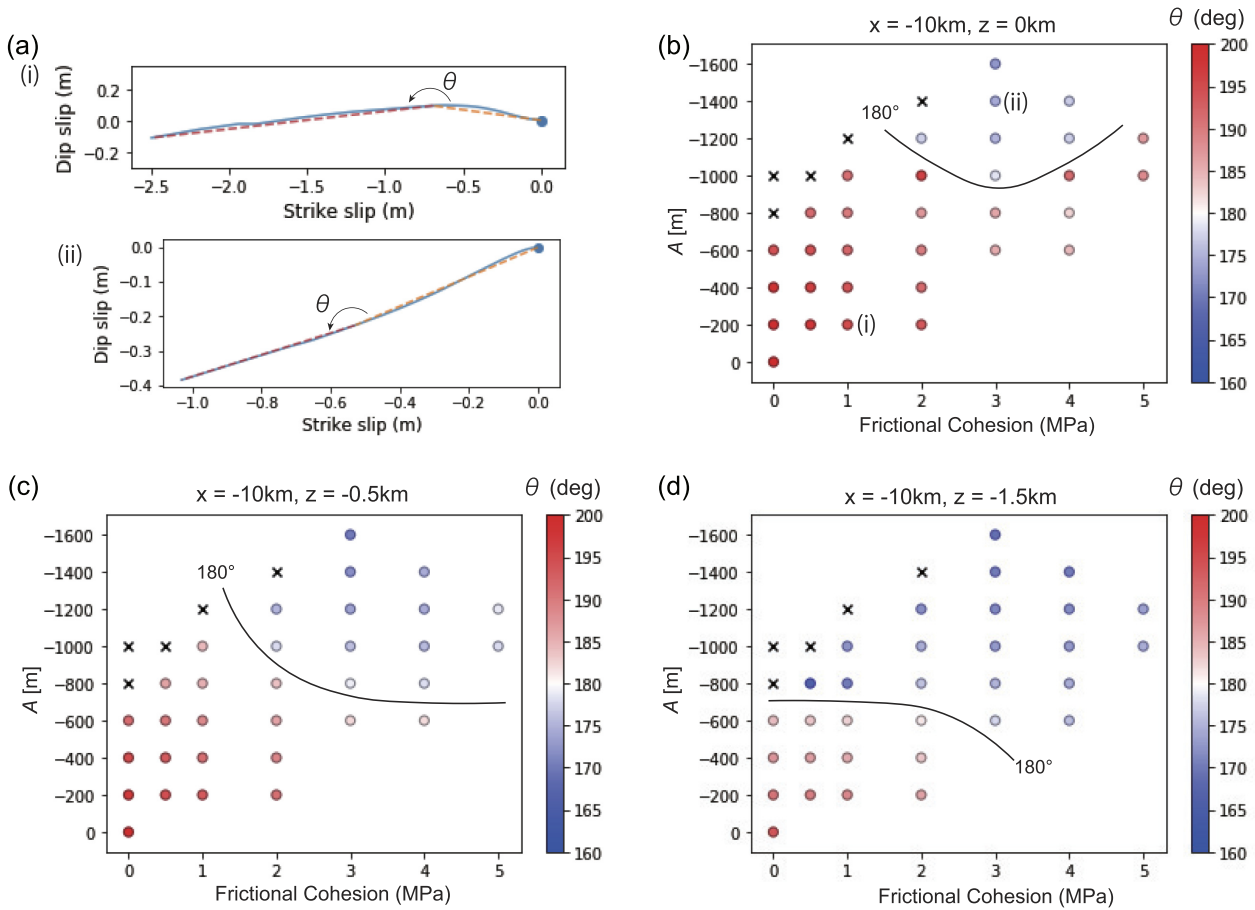
Figure 9. The dependence of slickenline curvature on model parameters in the cases with a non-planar fault and depth-dependent regional pre-stress. (a) Examples of synthetic slickenlines and the quantification of the main curvature of a slickenline. Using the method of least-square, we fit two straight lines (an orange line and a red line) to a curved slickenline and report the angle θ between these two lines. Panels (i) and (ii) show examples of line fitting. (b) Dependence of the curvature of slickenlines on the degree of non-planarity A and frictional cohesion C_0. A slickenline in each case is taken from location $(x, y, z) = (-10\,\text{km}, A, 0\,\text{km})$. Black crosses correspond to cases in which the rupture starts within the shallow, non-planar fault segment. Red dots show the cases with convex-up curvature (i.e. the same as in the planar fault model) and blue dots represent convex-down curvature (i.e. abnormal convexity). A black line shows an approximate contour for $\theta = 180^\circ$. (c) The same as in Fig. 9(b) except that slickenline in each case is taken from location $(x, y, z) = (-10\,\text{km}, A, -0.5\,\text{km})$. (d) The same as in Fig. 9(b) except that slickenline in each case is taken from location $(x, y, z) = (-10\,\text{km}, A, -1.5\,\text{km})$. For a wide range of model parameters, the occurrence of abnormal convexity (blue dots) near the Earth's surface is relatively rare, whereas, at depths, the parameter range that leads to abnormal convexity is wider.

For right-lateral strike-slip faults, the average angle $\bar{\theta}_0$ is zero, and hence the deviation angle is simply the local value of τ_{ds}^0/τ_{ss}^0. For dip-slip or oblique-slip faults, the value of $\Delta\theta_0$ may control the spatial pattern of slickenline convexity.

To demonstrate this concept, we rotate the regional stress tensor (eq. 3) by 45°:

$$\sigma\,[\text{MPa}] = \begin{pmatrix} -30.00 & \frac{29.38}{\sqrt{2}} & -30.00 \\ \frac{29.38}{\sqrt{2}} & -60.00 & \frac{29.38}{\sqrt{2}} \\ -30.00 & \frac{29.38}{\sqrt{2}} & -30.00 \end{pmatrix} \times \frac{|z|}{10\,\text{km}}, \tag{6}$$

which becomes optimal for a right-lateral, oblique-slip fault. Considering this stress tensor with the average angle $\bar{\theta}_0 = 45^\circ$, the local deviation angle $\Delta\theta_0(x, z)$ can be calculated as

$$\Delta\theta_0(x, z) = \tan^{-1}\left(\frac{\tau_z^0(x, z)}{\tau_x^0(x, z)}\right) - 45^\circ. \tag{7}$$

Fig. 14 shows the results of planar and rough fault models with the 45° rotated regional pre-stress. In the planar fault model, the spatial pattern of slickenline convexity can be understood as rotating the

right-lateral strike-slip fault case by 45° (Fig. 14a), consistent with the result of Kearse & Kaneko (2020). In the rough fault model, the regions in the mixed-mode directions at greater depths (>1 km) where the deviation angle $\Delta\theta_0$ is positively large result in abnormal slickenlines (i.e. slickenlines located on the red contours in Fig. 14b). Slickenlines at large negative $\Delta\theta_0$ lead to the enhancement of slickenline curvature, as expected (Fig. 14b). These results suggest that slickenline convexity on all fault types may be controlled by the direction of rupture propagation and the deviation of local pre-stress direction from the average value over the fault as defined by eq. (5).

6.5 Interpreting curved slickenlines from field observations

Our modelling results further support the idea that observations of coseismic slickenlines can be used to infer the rupture directions of earthquakes (Kearse & Kaneko 2020), assuming that the field data are collected from structurally simple parts of the fault with
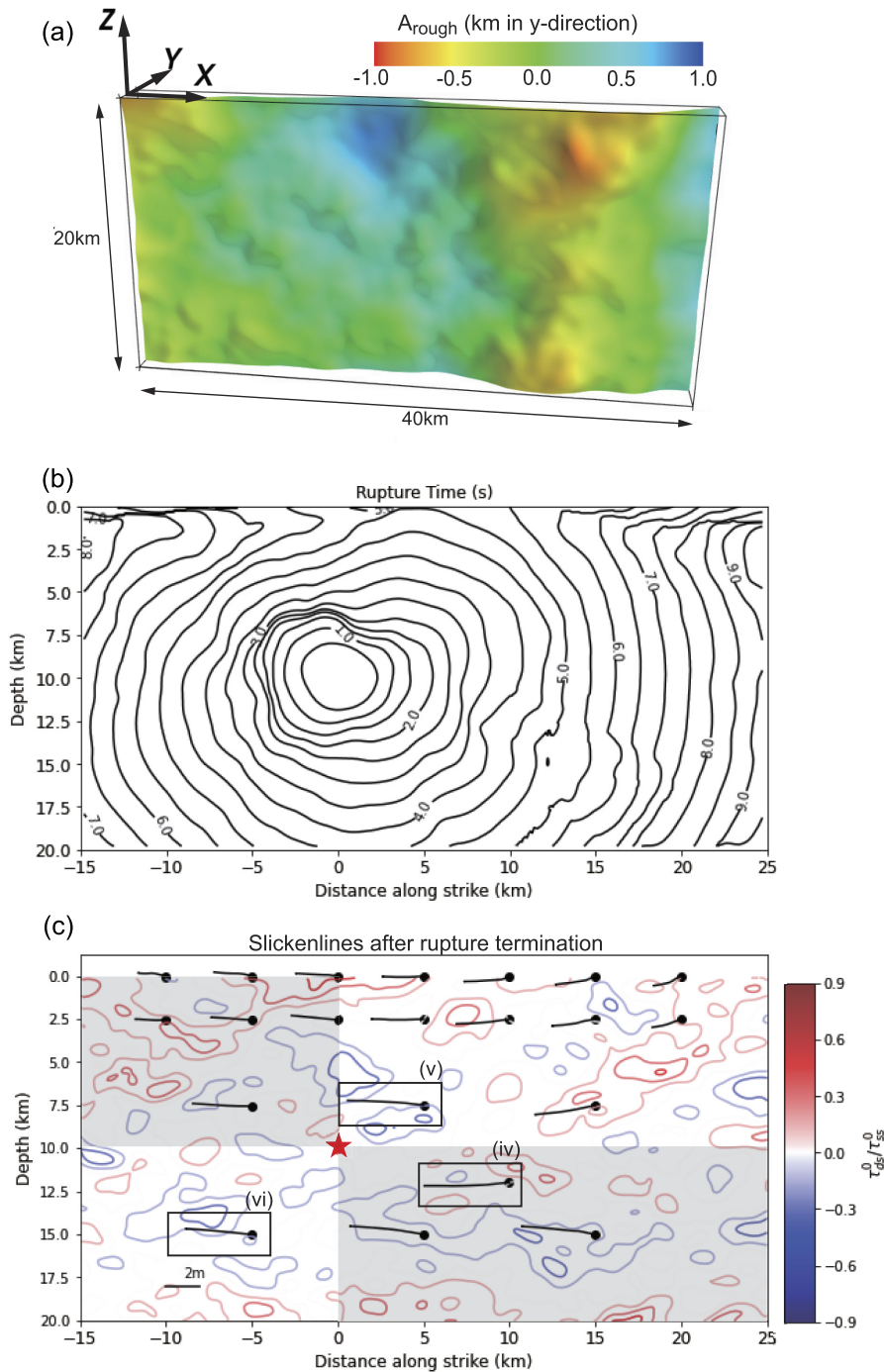
Figure 10. Model setup and the distribution of slickenlines on a rough fault with depth-dependent regional pre-stress. (a) The fault geometry. A_{rough} is defined as the position of the fault in the *y*-direction. (b) Rupture arrival time contour. Each contour represents the time (s) when the rupture front first arrives. (c) Synthetic slickenlines engraved on the far side of the fault in the rough fault model. Each black line is a slickenline calculated at each black dot on the fault plane. A red star shows the hypocentre. The colour contours represent the values of $\tau_{\text{ds}}^0/\tau_{\text{ss}}^0$. Grey and white areas show the region of convex-up and convex-down slickenline curvature expected in a planar fault model, respectively. Slickenlines in the black rectangular boxes are examples of abnormal convexity.

known dip directions. For example, if the rupture direction of the Kaikoura earthquake was unknown, the slickenlines observations (Fig. 1a) would have helped distinguish an earthquake scenario of nucleation in the northeast with westward rupture propagation from a nucleation in the southeast with eastward rupture propagation, as proposed by Kearse *et al.* (2019).

During surface-rupturing earthquakes, it is common for coseismic fault displacement at Earth's surface to produce a complex pattern of ground deformation tens to hundreds of meters wide. Within these swaths of broken ground, net displacement is commonly partitioned between discrete slip on multiple faults strands, distributed shear, up-buckling, fissure opening, local block rotation, and
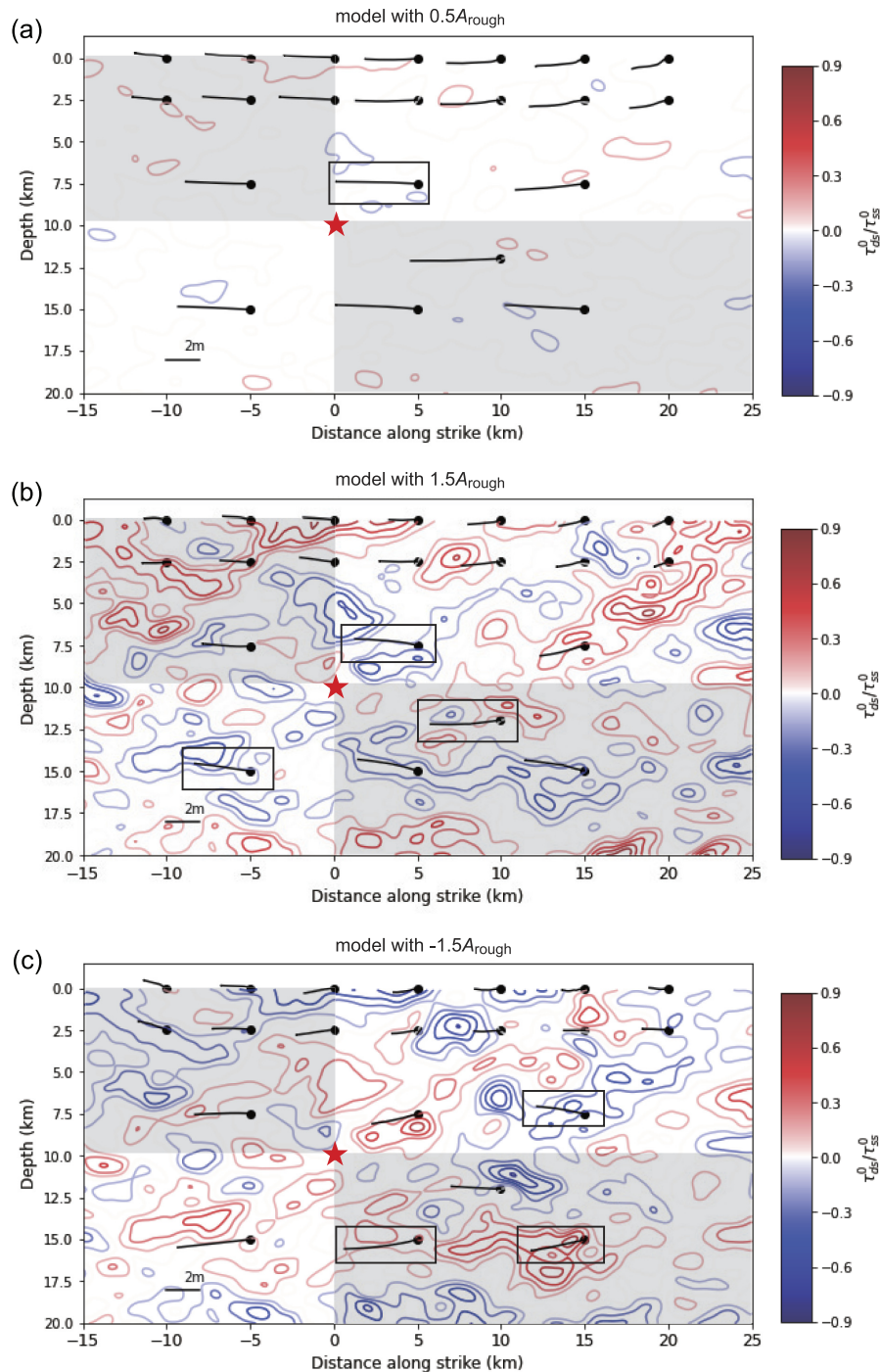
Figure 11. Distribution of slickenlines engraved on the far side of the fault in rough fault models with different degrees of fault roughness. (a) Synthetic slickenlines in the rough fault model with $0.5 \times A_{\text{rough}}$. (b) Synthetic slickenlines in the rough fault model with $1.5 \times A_{\text{rough}}$. (c) Synthetic slickenlines in the rough fault model with $-1.5 \times A_{\text{rough}}$. In these models, the slickenlines near the Earth's surface show the same convexity as in the planar fault, whereas slickenlines at depths located in the area of large positive $\tau_{\text{ds}}^0/\tau_{\text{ss}}^0$ show abnormal convexity. Slickenlines in the black rectangular boxes are examples of abnormal convexity.

subsidence of near-surface materials (Little *et al.* 2021; Kearse *et al.* 2018; Ponti *et al.* 2020). These processes can generate slickenlines on fault surfaces that may not be directly related to the local net slip vector, and instead record changes in coseismic slip direction that relate to the deformation of near-surface geology within the fault zone (Kearse *et al.* 2018). Accordingly, when using slickenlines to infer the kinematics or dynamics of ground-rupturing earthquakes,

data should be collected from on-fault locations where coseismic slip at the ground surface is focused across a single fault plane, so as to obtain a record of slip that is uncomplicated by secondary effects.

While our results demonstrate that abnormal convexity of slickenlines can be understood in the context of stress heterogeneities, the parameter space for which they occur is narrow. Moreover, the
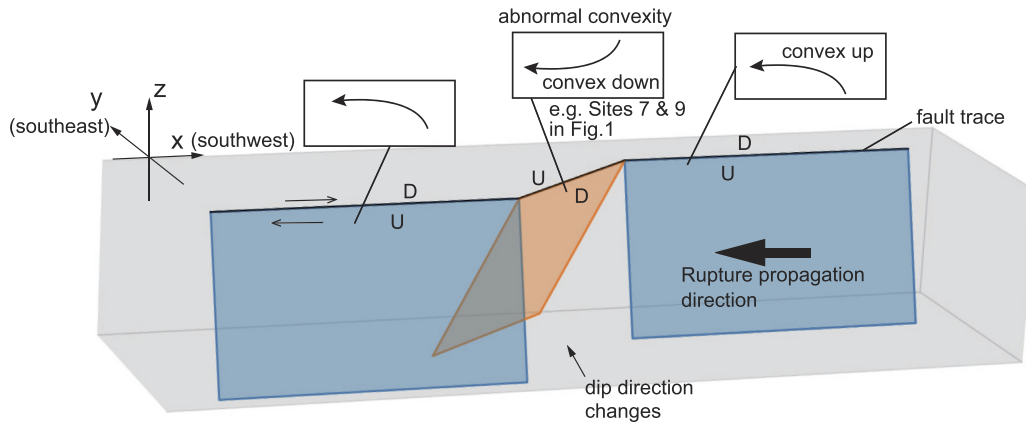
Figure 12. A schematic diagram of a part of the Kekerengu fault illustrating the relation between the fault geometry and slickenline convexity. Up (U) and down (D) are the relative vertical motion across the Kekerengu fault due to the Kaikoura earthquake (Fig. 1), and each box and arrow show the convexity of observed slickenlines engraved on the southeastern side of the fault plane. Abnormal convexity drawn in this figure corresponds to the observations at Sites 7 and 9 in Fig. 1(a). Abnormal convexity of slickenlines was observed where the fault dip angle changes locally (Kearse *et al.* 2019), consistent with what is expected from our numerical results. Note that the depth extent of the fault segment dipping southeast with abnormal convexity is unknown.
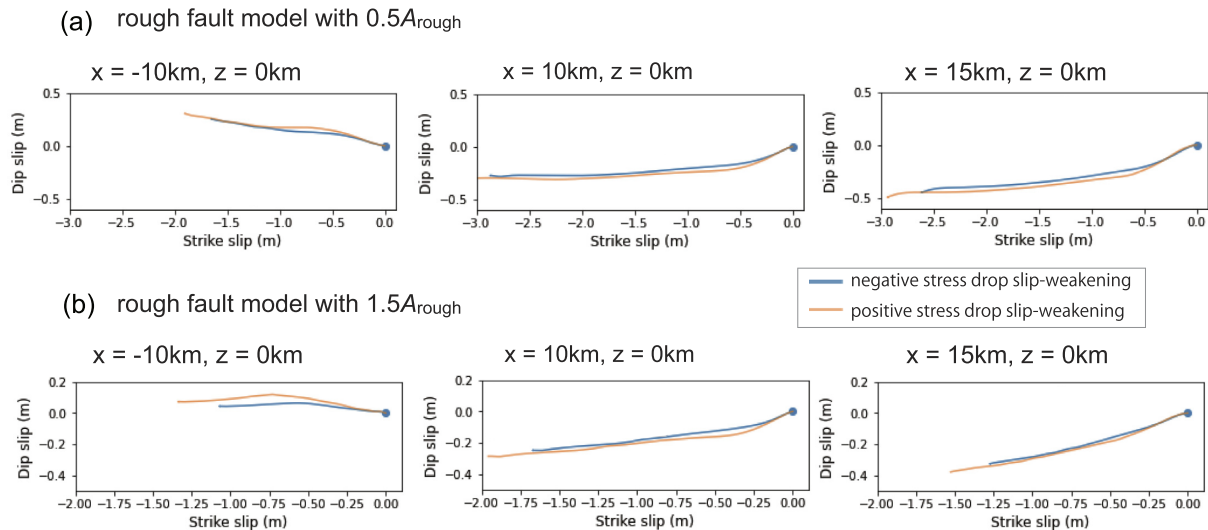

Figure 13. Synthetic slickenlines in the model with a negative stress-drop patch at shallow depths. (a) Slickenlines engraved on the far side of the fault from the rough fault model with $0.5 \times A_{rough}$ and with and without a patch of negative stress drop at a shallow depth (in the top 3 km). Blue curves show the result with a negative stress drop patch ($\mu_d = 0.5$ in the top 3 km). Orange curves show the result with positive stress drop, slip-weakening friction ($\mu_d = 0.373$ in the top 3 km). (b) The same as in Fig. 13(a) except that the degree of fault roughness is given by $1.5 \times A_{rough}$ which is the same as in Fig. 11(b). The blue lines are smoother than the orange lines, but the sense of convexity remains the same in these models.

structural conditions that favour the development of abnormal convexity, such as fault bends and stepovers, also promote the development of wider fault damage zones and structural complexity. These conditions are not favourable for the generation of slickenlines likely to record a simple and near complete history of single coseismic slip episode. However, these regions surrounding fault bends and stepovers are thought to host the nucleation and termination of earthquake ruptures (King & Nábělek 1985; Wesnousky 2006; Biasi & Wesnousky 2017). For this reason, they represent strategic locations to uncover palaeo rupture directions, and test earthquake gate models by sampling each side of a potential rupture barrier (Howarth *et al.* 2021). With these considerations, field data collection should focus on locations that straddle potential earthquake barriers, yet on structurally simple parts of the fault with known dip directions.

6.6 Model limitations

Several important assumptions are made in our model. First, the model assumes that the Earth's surface is flat and ignores the effect of topography. Since topography, such as the presence of a mountain range on one side of a dipping fault, may induce spatially non-uniform shear stresses on the fault, the resulting slickenline convexity may be influenced by the local topography. The shape of a free surface is also known to influence dynamic stresses at the propagating rupture front (e.g. Zhang *et al.* 2016) and may influence the curvature of slickenlines. Secondly, depth-dependent elastic properties of the wall rocks could complicate the rupture dynamics and resulting slickenline curvature (Macklin *et al.* 2021). Third, we assume slip-weakening fault friction for simplicity, and
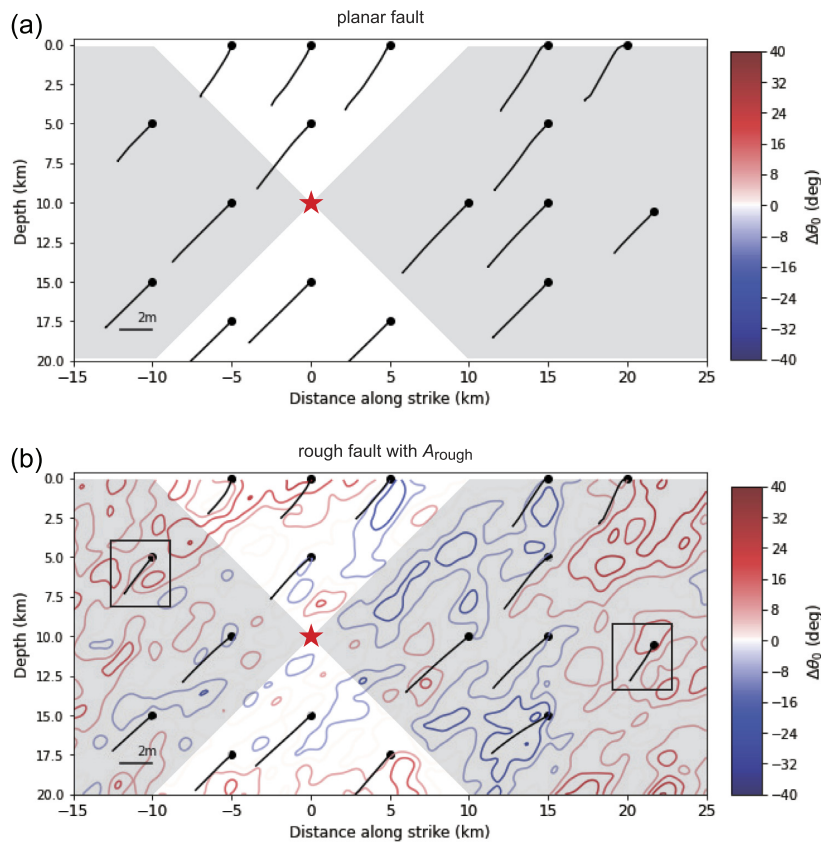
Figure 14. Slickenlines on the planar and rough fault models with 45° rotated, depth-dependent regional pre-stress. (a) Slickenlines engraved on the far side of the fault in the planar fault model with 45° rotated regional pre-stress. Each black line shows a slickenline. A red star shows the hypocentre. Grey and white areas show the region of convex-up and convex-down slickenline curvature expected in a planar fault model, respectively. The colour contour depicts the deviation angle $\Delta\theta_0$ (°) of local fault non-planarity, with $\Delta\theta_0 = 0$ for the planar fault. The convexity of slickenlines follows the spatial pattern of white and grey areas. (b) Slickenlines on the rough fault model with 45° rotated regional pre-stress and A_{rough} shown in Fig. 10(a). Slickenlines in the black rectangular boxes are examples of abnormal convexity.

do not consider other types of friction laws, such as rate-and-state friction (Dieterich 1979; Ruina 1983) with enhanced weakening at coseismic slip rates (e.g. Rice 2006). How and to what extent different friction laws influence the curvature and/or convexity of slickenlines remains unclear. Fourth, we ignore the effect of inelastic, distributed deformation, which may be modelled in the framework of off-fault plasticity (e.g. Andrews 2005; Ma 2008; Kaneko & Fialko 2011; Roten et al. 2017). As mentioned above, interpretations of observed slickenlines should focus on structurally simple parts of a fault where a majority of deformation is localized on main fault strands. Investigating the effects of topography, different friction laws and inelastic deformation on the characteristics of slickenlines remains a subject of future work.

6.7 Difficulty in the estimation of absolute stress level from curved slip path

Spudich et al. (1998) and Guatteri & Spudich (1998) found that the degree of temporal rake rotation on a planar fault, which is induced by dynamic stress changes in the cohesive zone, is sensitive to the absolute stress level. Their result indicates that observational methods (e.g. kinematic slip inversion) that can retrieve the temporal evolution of slip path at depth may be used to infer the absolute stress level. At the same time, retrieving temporal changes in the rake angle at depth during a large earthquake is generally considered

difficult due to large uncertainty and non-uniqueness associated with source inversion (e.g. Konca et al. 2013; Mai et al. 2016). In our models with non-planar and rough faults, we show that the degree of slickenline curvature also depends significantly on the change in local fault geometry. Hence without prior knowledge of the fault geometry at depth, it would be more difficult to infer the absolute level of stress at depth from the inferences of curved slip path.

7 CONCLUSIONS

Using simulations of dynamic ruptures, we have investigated the effect of non-planar fault geometry on the characteristics and spatial patterns of coseismic slickenlines. We have found that a non-planar fault model can lead to the convexity of slickenlines opposite from that of the planar fault model. Non-planar strike-slip faults combined with a homogeneous tectonic stress field induce local pre-stress heterogeneities, causing the slickenlines to have abnormal convexity under certain conditions. This effect is notable where the fault dip angle changes locally along the strike. We have also explored a wide range of stress conditions and friction parameters and showed that the parameter space for which abnormal convexity of slickenlines occurs near the Earth's surface is narrow. Nonetheless, slickenlines on geometrically complex faults need to be carefully interpreted and investigation of rupture direction using curved

slickenlines should focus on structurally simple parts of faults with known dip directions.

DATA AVAILABILITY

Numerical data used to create all the figures are available at https://doi.org/10.5281/zenodo.7014402. The computer code used in this work was developed by Ampuero (2002) and Kaneko *et al.* (2008).

REFERENCES

Ammon, C.J., Velasco, A.A. & Lay, T., 1993. Rapid estimation of rupture directivity: application to the 1992 landers (ms = 7.4) and Cape Mendocino (ms = 7.2), California earthquakes, *Geophys. Res. Lett.,* **20**(2), 97–100.

Ampuero, J.-P., 2002. Etude physique et numérique de la nucléation des séismes, *PhD thesis*, Univ. Paris 7, Denis Diderot, Paris.

Ando, R. & Kaneko, Y., 2018. Dynamic rupture simulation reproduces spontaneous multifault rupture and arrest during the 2016 Mw 7.9 Kaikoura earthquake, *Geophys. Res. Lett.,* **45**(23), 12–875.

Andrews, D.J., 2005. Rupture dynamics with energy loss outside the slip zone, *J. geophys. Res.,* **110**(B1), doi:10.1029/2004JB003191.

Andrews, D.J. & Barall, M., 2011. Specifying initial stress for dynamic heterogeneous earthquake source models, *Bull. seism. Soc. Am.,* **101**(5), 2408–2417.

Andrews, D.J. & Ben-Zion, Y., 1997. Wrinkle-like slip pulse on a fault between different materials, *J. geophys. Res.,* **102**, 553–571.

Biasi, G.P. & Wesnousky, S.G., 2017. Bends and ends of surface ruptures, *Bull. seism. Soc. Am.,* **107**(6), 2543–2560.

Day, S.M., Dalguer, L.A., Lapusta, N. & Liu, Y., 2005. Comparison of finite difference and boundary integral solutions to three-dimensional spontaneous rupture, *J. geophys. Res.,* **110**(B12), doi:10.1029/2005JB003813.

Dieterich, J.H., 1979. Modeling of rock friction: 1. Experimental results and constitutive equations, *J. geophys. Res.,* **84**, 2161–2168.

Dunham, E.M., Belanger, D., Cong, L. & Kozdon, J.E., 2011. Earthquake ruptures with strongly rate-weakening friction and off-fault plasticity, Part 2: nonplanar faults, *Bull. seism. Soc. Am.,* **101**(5), 2308–2322.

Fliss, S., Bhat, H.S., Dmowska, R. & Rice, J.R., 2005. Fault branching and rupture directivity, *J. geophys. Res.,* **110**(B6), doi:10.1029/2004JB003368.

Gomberg, J., Reasenberg, P., Bodin, P.l. & Harris, R., 2001. Earthquake triggering by seismic waves following the landers and hector mine earthquakes, *Nature,* **411**(6836), 462–466.

Guatteri, M. & Spudich, P., 1998. Coseismic temporal changes of slip direction: the effect of absolute stress on dynamic rupture, *Bull. seism. Soc. Am.,* **88**(3), 777–789.

Harris, R.A. & Day, S.M., 1999. Dynamic 3D simulations of earthquakes on en echelon faults, *Geophys. Res. Lett.,* **26**(14), 2089–2092.

Harris, R.A. & Day, S.M., 2005. Material contrast does not predict earthquake rupture propagation direction, *Geophys. Res. Lett.,* **32**(23), doi:10.1029/2005GL023941.

Harris, R.A. *et al.*, 2018. A suite of exercises for verifying dynamic earthquake rupture codes, *Seismol. Res. Lett.,* **89**(3), 1146–1162.

Holden, C., Kaneko, Y., D'Anastasio, E., Benites, R., Fry, B. & Hamling, I.J., 2017. The 2016 Kaikōura earthquake revealed by kinematic source inversion and seismic wavefield simulations: slow rupture propagation on a geometrically complex crustal fault network, *Geophys. Res. Lett.,* **44**(22), 11 320–11 328.

Howarth, J.D. *et al.*, 2021. Spatiotemporal clustering of great earthquakes on a transform fault controlled by geometry, *Nat. Geosci.,* **14**(5), 314–320.

Ida, Y., 1972. Cohesive force across the tip of a longitudinal-shear crack and Griffith's specific surface energy, *J. geophys. Res.,* **77**, 3796–3805.

Kaneko, Y. & Fialko, Y., 2011. Shallow slip deficit due to large strike-slip earthquakes in dynamic rupture simulations with elasto-plastic off-fault response, *Geophys. J. Int.,* **186**, 1389–1403.

Kaneko, Y. & Lapusta, N., 2010. Supershear transition due to a free surface in 3-D simulations of spontaneous dynamic rupture on vertical strike-slip faults, *Tectonophysics,* **493**, 272–284.

Kaneko, Y., Lapusta, N. & Ampuero, J.-P., 2008. Spectral element modeling of spontaneous earthquake rupture on rate and state faults: effect of velocity-strengthening friction at shallow depths, *J. geophys. Res.,* **113**(B9), doi:10.1029/2007JB005553.

Kearse, J. & Kaneko, Y., 2020. On-fault geological fingerprint of earthquake rupture direction, *J. geophys. Res.,* **125**(9), e2020JB019863, doi:10.1029/2020JB019863.

Kearse, J. *et al.*, 2018. Onshore to offshore ground-surface and seabed rupture of the Jordan–Kekerengu–Needles Fault Network during the 2016 Mw 7.8 Kaikōura Earthquake, New Zealand, *Bull. seism. Soc. Am.,* **108**(3B), 1573–1595.

Kearse, J., Kaneko, Y., Little, T. & Van Dissen, R., 2019. Curved slickenlines preserve direction of rupture propagation, *Geology,* **47**(9), 838–842.

King, G. & Nábělek, J., 1985. Role of fault bends in the initiation and termination of earthquake rupture, *Science,* **228**(4702), 984–987.

Klinger, Y. *et al.*, 2018. Earthquake damage patterns resolve complex rupture processes, *Geophys. Res. Lett.,* **45**(19), 10279–10287.

Kobayashi, H., Koketsu, K. & Miyake, H., 2017. Rupture processes of the 2016 Kumamoto earthquake sequence: causes for extreme ground motions, *Geophys. Res. Lett.,* **44**(12), 6002–6010.

Konca, O.A., Kaneko, Y., Lapusta, N. & Avouac, J.-P., 2013. Kinematic inversion of physically plausible earthquake source models obtained from dynamic rupture simulations, *Bull. seism. Soc. Am.,* **103**(5), 2621–2644.

Little, T., Morris, P., Hill, M., Kearse, J., Van Dissen, R., Manousakis, J., Zekkos, D. & Howell, A., 2021. Coseismic deformation of the ground during large-slip strike-slip ruptures: finite evolution of "mole tracks", *Geosphere,* **17**(4), 1170–1192.

Ma, S., 2008. A physical model for widespread near-surface and fault zone damage induced by earthquakes, *Geochem. Geophys. Geosyst.,* **9**(11), doi:10.1029/2008GC002231.

Macklin, C., Kaneko, Y. & Kearse, J., 2021. Coseismic slickenlines record the emergence of multiple rupture fronts during a surface-breaking earthquake, *Tectonophysics,* **808**, doi:10.1016/j.tecto.2021.228834.

Mai, P.M. *et al.*, 2016. The earthquake-source inversion validation (SIV) project, *Seismol. Res. Lett.,* **87**(3), 690–708.

Marone, C., 1998. Laboratory-derived friction laws and their application to seismic faulting, *Annu. Rev. Earth planet. Sci.,,* **26**, 643–696.

Marone, C., Scholz, C.H. & Bilham, R., 1991. On the mechanics of earthquake afterslip, *J. geophys. Res.,* **96**, 8441–8452.

McGuire, J.J., Zhao, L. & Jordan, T.H., 2002. Predominance of unilateral rupture for a global catalog of large earthquakes, *Bull. seism. Soc. Am.,* **92(8)**, 3309–3317.

Otsubo, M., Shigematsu, N., Imanishi, K., Ando, R., Takahashi, M. & Azuma, T., 2013. Temporal slip change based on curved slickenlines on fault scarps along Itozawa fault caused by 2011 Iwaki earthquake, northeast Japan, *Tectonophysics,* **608**, 970–979.

Otsuki, K., Minagawa, J., Aono, M. & Ohtake, M., 1997. On the curved striations of Nojima seismic fault engraved at the 1995 Hyogoken-Nambu earthquake, Japan, *J. Seismol. Soc. Jpn.,* **49**, 451–460.

Palmer, A.C. & Rice, J.R., 1973. The growth of slip surfaces in the progressive failure of over-consolidated clay, *Proc. R. Soc. Lond., A,* **332**, 527–548.

Perrin, C., Manighetti, I. & Gaudemer, Y., 2016. Off-fault tip splay networks: a genetic and generic property of faults indicative of their long-term propagation, *Comp. Rend. Geosci.,* **348**(1), 52–60.

Pitarka, A., Dalguer, L.A., Day, S.M., Somerille, P.G. & Dan, K., 2009. Numerical study of ground-motion differences between buried-rupturing and surface-rupturing earthquakes, *Bull. seism. Soc. Am.,* **99,** 1521–1537.

Ponti, D.J. *et al.*, 2020. Documentation of surface fault rupture and ground-deformation features produced by the 4 and 5 July 2019 Mw 6.4 and Mw 7.1 Ridgecrest Earthquake Sequence, *Seismol. Res. Lett.,* **91**(5), 2942–2959.

Rice, J.R., 2006. Heating and weakening of faults during earthquake slip, *J. geophys. Res.,* **111**(B5), doi:10.1029/2005JB004006.

Roten, D., Olsen, K.B. & Day, S.M., 2017. Off-fault deformations and shallow slip deficit from dynamic rupture simulations with fault zone plasticity, *Geophys. Res. Lett.,* **44**(15), 7733–7742.

Ruina, A.L., 1983. Slip instability and state variable friction laws, *J. geophys. Res.,* **88,** 10 359–10 370.

Shi, Z. & Day, S.M., 2013. Rupture dynamics and ground motion from 3-D rough-fault simulations, *J. geophys. Res.,* **118**(3), 1122–1141.

Somerville, P.G., Smith, N.F., Graves, R.W. & Abrahamson, N.A., 1997. Modification of empirical strong ground motion attenuation relations to include the amplitude and duration effects of rupture directivity, *Seismol. Res. Lett.,* **68**(1), 199–222.

Spudich, P., Guatteri, M., Otsuki, K. & Minagawa, J., 1998. Use of fault striations and dislocation models to infer tectonic shear stress during the 1995 Hyogo-Ken Nanbu (Kobe) earthquake, *Bull. seism. Soc. Am.,* **88**(2), 413–427.

Wesnousky, S.G., 2006. Predicting the endpoints of earthquake ruptures, *Nature,* **444,** 358–360.

Yoshida, S., Koketsu, K., Shibazaki, B., Sagiya, T., Kato, T. & Yoshida, Y., 1996. Joint inversion of near- and far-field waveforms and geodetic data for the rupture process of the 1995 Kobe earthquake, *J. Phys. Earth,* **44**(5), 437–454.

Zhang, Z., Xu, J. & Chen, X., 2016. The supershear effect of topography on rupture dynamics, *Geophys. Res. Lett.,* **43**(4), 1457–1463.

APPENDIX A: LINEAR SLIP-WEAKENING FRICTION LAW AND NUMERICAL RESOLUTION

We assume that the constitutive response of a fault is governed by a linear slip-weakening friction law (Ida 1972; Palmer & Rice 1973). We follow the implementation procedure of a linear slip-weakening friction law as described in benchmark problem TPV28 of Harris *et al.* (2018). The shear strength on the fault τ_{strength} is given by

$$\tau_{\mathrm{strength}} = C_0 + \mu\sigma_n , \qquad\qquad (A1)$$

where C_0 and σ_n are the frictional cohesion and the effective normal stress, respectively. In the slip-weakening friction law, the friction coefficient μ decreases from its static value μ_s to a dynamic value μ_d over a characteristic distance d_c. When the local fault slip is D, the time-varying friction coefficient μ is given by

$$\mu = \mu_s + (\mu_d - \mu_s)\min(D/d_c, 1) . \qquad\qquad (A2)$$

An important characteristic of numerical solutions to dynamic rupture problems is the resolution of a cohesive zone. To resolve the cohesive zone, the ratio $\Lambda/\Delta x$ of the cohesive zone size Λ to the average node spacing Δx needs to be at least 3–5 (Day *et al.* 2005; Kaneko & Lapusta 2010). In this study, we set $\Delta x = 100$ m, and the corresponding value of Λ is ≈ 500 m, leading to $\Lambda/\Delta x > 3$ in our simulations. In addition, we consider a model with the average node spacing of $\Delta x = 50$ m, which gives the result nearly identical to the case with $\Delta x = 100$ m (Fig. A1). Hence we conclude that $\Delta x = 100$ m is sufficient in this study. For $\Delta x = 100$ m, each simulation takes 1.0 - 3.5 hours on 180 cores on the FUJITSU Supercomputer (Wisteria/BDEC01, Odyssey) in the Information Technology Center, the University of Tokyo.
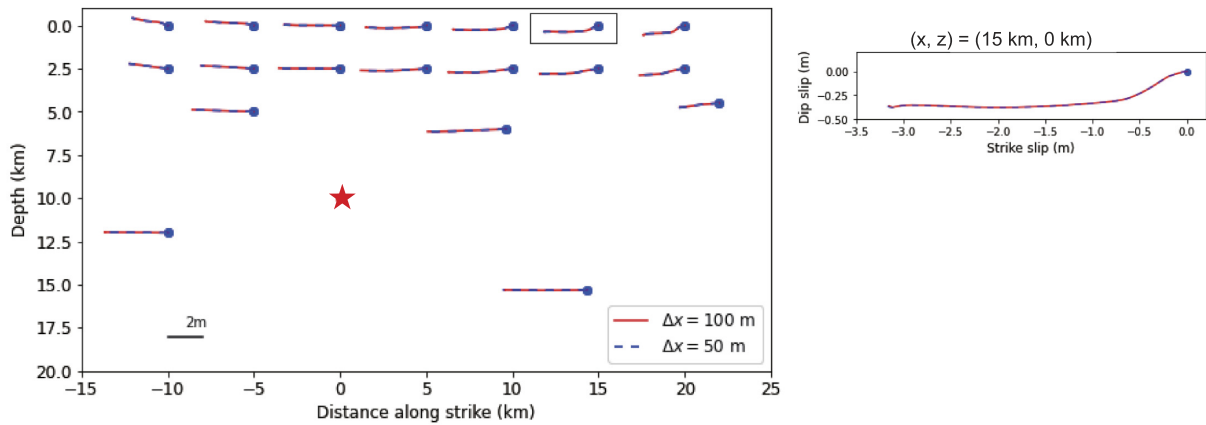

Figure A1. Synthetic slickenlines in models with the average node spacing of 100 m (red lines) and 50 m (blue dashed lines). These results correspond to planar faults with depth-dependent regional pre-stress. The initial stress tensor is the same as the models in Section 5. Red lines ($\Delta x = 100$ m) and blue dashed lines ($\Delta x = 50$ m) are virtually identical.
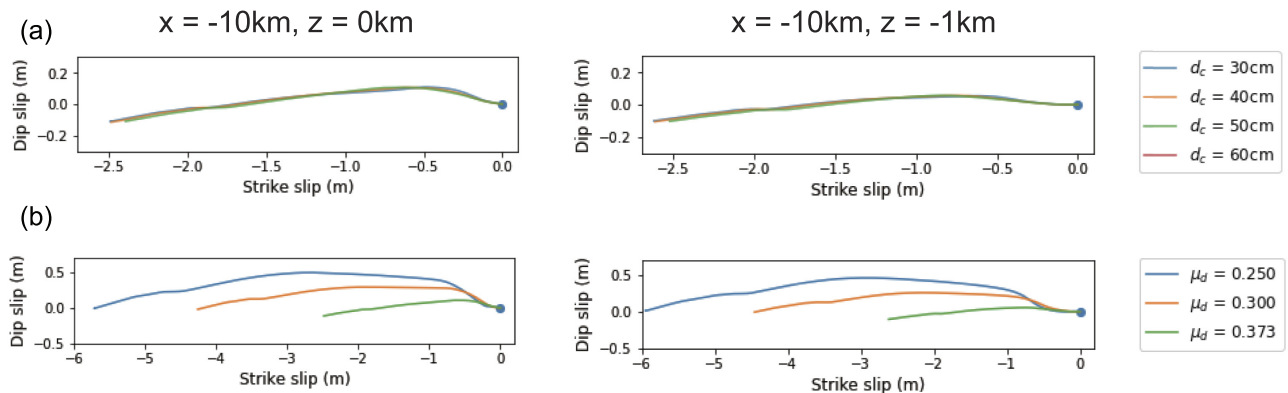

Figure A2. Dependence of slickenline curvature on parameters d_c and μ_d in the non-planar fault model with depth-dependent regional pre-stress. We assume $A = -400$ m and $C_0 = 1$ MPa and slickenlines are taken from location $(x, y, z) = (-10\,\mathrm{km}, A, 0\,\mathrm{km})$ and $(-10\,\mathrm{km}, A, -1\,\mathrm{km})$. (a) The dependence of slickenline curvature on d_c. Increasing d_c leads to a slightly smaller total slip, but the shape of slickenlines does not change. (b) The dependence of slickenline curvature on μ_d. Larger μ_d leads to larger total slip and different slickenline curvature, but the convexity of the slickenline remains unchanged.

APPENDIX B: MODEL SET-UP OF NON-PLANAR FAULT WITH UNIFORM REGIONAL PRE-STRESS

We assume a uniform, initial stress tensor given by

$$\sigma \, [\text{MPa}] = \begin{pmatrix} \sigma_{11} & \sigma_{12} & \sigma_{13} \\ \sigma_{12} & \sigma_{22} & \sigma_{23} \\ \sigma_{13} & \sigma_{23} & \sigma_{33} \end{pmatrix} = \begin{pmatrix} -60.00 & 29.38 & 0 \\ 29.38 & -60.00 & 0 \\ 0 & 0 & 0 \end{pmatrix}. \tag{B1}$$

To simulate a 3-D shape of the non-planar fault (e.g. Fig. 3), we define the following variables:

$$x_1 = x + 10\,\text{km}, \qquad x_2 = x + 20\,\text{km}, \qquad z_1 = z_2 = z_3 = z - 1.5\,\text{km} \tag{B2}$$

$$r_1 = \sqrt{x_1^2 + z_1^2}, \qquad r_2 = \sqrt{x_2^2 + z_2^2}, \qquad r_3 = |z_3| \tag{B3}$$

$$R = 1.5\,\text{km}, \qquad R' = 2R = 3\,\text{km}, \tag{B4}$$

where R is the depth extent of non-planar fault segment. The non-planar fault geometry is characterized by

$$y = f(x, z) = \begin{cases} A(1 + \cos(\pi r_1 / R')) & (r_1 < R') \\ A(1 + \cos(\pi r_2 / R')) & (r_2 < R') \\ A(1 + \cos(\pi r_3 / R')) & (-20\,\text{km} < x < -10\,\text{km}, \; -1.5\,\text{km} < z \le 0\,\text{km}) \\ 0 & (\text{otherwise}) \end{cases} \tag{B5}$$

where A is the amplitude of the displaced fault at the Earth's surface along the y-direction. In this case, the partial derivatives of $f(x, z)$ are

$$f_x = \frac{\partial f(x, z)}{\partial x} = \begin{cases} -\pi \frac{A x_1}{r_1 R'} \sin(\pi r_1 / R') & (0 < r_1 < R') \\ -\pi \frac{A x_2}{r_2 R'} \sin(\pi r_2 / R') & (0 < r_2 < R') \\ 0 & (\text{otherwise}) \end{cases} \tag{B6}$$

and

$$f_z = \frac{\partial f(x, z)}{\partial z} = \begin{cases} -\pi \frac{A z_1}{r_1 R'} \sin(\pi r_1 / R') & (0 < r_1 < R') \\ -\pi \frac{A z_2}{r_2 R'} \sin(\pi r_2 / R') & (0 < r_2 < R') \\ -\pi \frac{A}{R'} \sin(\pi r_3 / R') & (-20\,\text{km} < x < -10\,\text{km}, \; -1.5\,\text{km} < z \le 0\,\text{km}) \\ 0 & (\text{otherwise}) \end{cases} \tag{B7}$$

We define h_1 and h_2 as

$$h_1 = \frac{1}{\sqrt{1 + f_x^2}}, \qquad h_2 = \frac{1}{\sqrt{1 + f_x^2 + f_z^2}}. \tag{B8}$$

Then the initial along-strike shear stress τ_{ss}, along-dip shear stress τ_{ds} and effective normal stress σ_n on the fault can be expressed as

$$\tau_{\text{ss}} = h_1 h_2 (-f_x \sigma_{11} - f_z \sigma_{13} + (1 - f_x^2) \sigma_{12} - f_x f_z \sigma_{23} + f_x \sigma_{22}) \tag{B9}$$

$$\begin{aligned} \tau_{\text{ds}} = -h_1 h_2^2 (f_x^2 f_z \sigma_{11} - (1 + f_x^2 - f_z^2) f_x \sigma_{13} - 2 f_x f_z \sigma_{12} \\ - (1 + f_x^2) f_z \sigma_{33} + (1 + f_x^2 - f_z^2) \sigma_{23} + f_z \sigma_{22}) \end{aligned} \tag{B10}$$

$$\sigma_n = h_2^2 (-f_x^2 \sigma_{11} - 2 f_x f_z \sigma_{13} + 2 f_x \sigma_{12} - f_z^2 \sigma_{33} + 2 f_z \sigma_{23} - \sigma_{22}). \tag{B11}$$

To initiate rupture, we apply an additional shear stress τ_{nuke} within a circular zone of a 2.0-km radius around the hypocentre. τ_{nuke} is given

$$\tau_{\text{nuke}} [\text{MPa}] = \begin{cases} 11.60 & (r \le 1.4\,\text{km}) \\ 5.80(1 + \cos(\pi(r - 1.4\,\text{km})/600\,\text{m})) & (1.4\,\text{km} \le r \le 2\,\text{km}) \\ 0 & (\text{otherwise}) \end{cases}. \tag{B12}$$

where r represents the distance from the hypocentre along the fault plane.

APPENDIX C: MODEL SET-UP OF NON-PLANAR FAULT WITH DEPTH-DEPENDENT REGIONAL PRE-STRESS

In this scenario, we make the same assumptions as in the model of non-planar with a uniform regional pre-stress, except for the regional pre-stress, the fault geometry and the location of the hypocentre. We consider depth-dependent regional pre-stress given by

$$\sigma \, [\text{MPa}] = \begin{pmatrix} \sigma_{11} & \sigma_{12} & \sigma_{13} \\ \sigma_{12} & \sigma_{22} & \sigma_{23} \\ \sigma_{13} & \sigma_{23} & \sigma_{33} \end{pmatrix} = \begin{pmatrix} -60.00 & 29.38 & 0 \\ 29.38 & -60.00 & 0 \\ 0 & 0 & 0 \end{pmatrix} \times \frac{|z|}{7.5\,\text{km}}. \tag{C1}$$

The fault geometry is parametrized by the following variables.

$$x_1 = x + 10\,\text{km}, \qquad x_2 = x + 20\,\text{km}, \qquad z_1 = z_2 = z_3 = z \tag{C2}$$

$$r_1 = \sqrt{x_1^2 + z_1^2}, \qquad r_2 = \sqrt{x_2^2 + z_2^2}, \qquad r_3 = |z_3| \tag{C3}$$

$$R = 3\,\text{km}. \tag{C4}$$

The non-planar geometry is characterized by

$$y = f(x, z) = \begin{cases} \frac{A}{2}(1 + \cos(\pi r_1/R)) & (r_1 < R) \\ \frac{A}{2}(1 + \cos(\pi r_2/R)) & (r_2 < R) \\ \frac{A}{2}(1 + \cos(\pi r_3/R)) & (-20\,\text{km} < x < -10\,\text{km}, \ -3\,\text{km} < z \le 0\,\text{km}) \\ 0 & (\text{otherwise}) \end{cases} \tag{C5}$$

with the partial derivatives

$$f_x(x, z) = \begin{cases} -\pi \frac{A x_1}{2 r_1 R} \sin(\pi r_1/R) & (0 < r_1 < R) \\ -\pi \frac{A x_2}{2 r_2 R} \sin(\pi r_2/R) & (0 < r_2 < R) \\ 0 & (\text{otherwise}) \end{cases} \tag{C6}$$

$$f_z(x, z) = \begin{cases} -\pi \frac{A z_1}{2 r_1 R} \sin(\pi r_1/R) & (0 < r_1 < R) \\ -\pi \frac{A z_2}{2 r_2 R} \sin(\pi r_2/R) & (0 < r_2 < R) \\ -\pi \frac{A}{2 R} \sin(\pi r_3/R) & (-20\,\text{km} < x < -10\,\text{km}, \ -3\,\text{km} < z \le 0\,\text{km}) \\ 0 & (\text{otherwise}) \end{cases} \tag{C7}$$

The corresponding initial shear stresses τ_{ss} and τ_{ds}, and effective normal stress σ_n can be calculated by eqs (B9), (B10) and (B11), respectively. In order to set the initial stress at the hypocentre the same as in the model with uniform regional pre-stress, we assume the hypocentre at the depth of 7.5 km. We apply an additional shear stress τ_{nuke} within a circular zone of a 2.0-km radius around the hypocentre, using eq. (B12).

APPENDIX D: MODEL SET-UP OF ROUGH FAULT WITH DEPTH-DEPENDENT REGIONAL PRE-STRESS

We consider a 40 km by 20 km, vertical strike-slip fault embedded in an elastic half-space. The fault roughness is characterized by a self-similar fractal function. The Fourier spectrum of a 2-D self-affine function is a power law in wavenumber and is given by $P(k) \propto k^{-(2H+2)}$, where k is the magnitude of the 2-D wavenumber vector and H is the Hurst exponent. For a self-similar distribution, the Hurst exponent $H = 1$. The wavelength is $\lambda = 1/k$, and the amplitude of self-similar fault roughness becomes $A \propto \lambda^2 = k^{-2}$ (Andrews & Barall 2011; Shi & Day 2013). We make the surface with randomly selected sine waves and put them together by a linear superposition. Each sine waves have 1000–40 000 m wavelengths and their amplitudes are the square of the wavelength. The surface is smoothed by a moving-average filter with a radius of 1000 m.

Following Shi & Day (2013), the RMS roughness of the 2-D profiles h_{rms} is given by

$$h_{rms} = \left\{ \frac{1}{N_x N_z} \sum_{nz=0}^{N_z-1} \sum_{nx=0}^{N_x-1} [y(nx, nz) - \bar{h}]^2 \right\}^{1/2} \tag{D1}$$

$$\bar{h} = \frac{1}{N_x N_z} \sum_{nz=0}^{N_z-1} \sum_{nx=0}^{N_x-1} y(nx, nz), \tag{D2}$$

where N_x and N_z are the grid number of the 2-D fault surface parallel and perpendicular to the along-strike direction, respectively. In our rough fault model shown in Fig. 10, $h_{rms} = 10^{-2.1} L$, where L is the along-strike length of the fault.

We assume depth-dependent regional pre-stress given by

$$\sigma\,[\text{MPa}] = \begin{pmatrix} \sigma_{11} & \sigma_{12} & \sigma_{13} \\ \sigma_{12} & \sigma_{22} & \sigma_{23} \\ \sigma_{13} & \sigma_{23} & \sigma_{33} \end{pmatrix} = \begin{pmatrix} -60.00 & 29.38 & 0 \\ 29.38 & -60.00 & 0 \\ 0 & 0 & 0 \end{pmatrix} \times \frac{|z|}{10\,\text{km}}. \tag{D3}$$

The corresponding initial shear stresses and effective normal stress on the rough fault are calculated using (B9), (B10) and (B11), respectively.